Università degli Studi di Padova
Dipartimento di Fisica e Astronomia "Galileo Galilei"

Corso di Laurea in Fisica

Design of an electrostatic probe system for the NIO1 experiment

Laureanda:
Alessia Scriminich

Relatore: Dott. Gianluigi Serianni
Correlatore: Dott.ssa Monica Spolaore

Anno Accademico 2014/2015

Abstract

The NIO1 experiment is a compact and modular negative ion source built at Consorzio RFX, Padua, with the aim to investigate the optimal configuration for a negative ion source of the type needed for the nuclear fusion experiment ITER. In this perspective, a thorough diagnostics of the NIO1 source is essential. The present thesis aims at the design of a system of two electrostatic probes which will scan the source along two orthogonal directions, providing profiles of electron density and temperature. The work starts with a study of the requirements on the probe design imposed by the nature of the plasma in the source: probe dimension is optimised by studying simulated electron density and temperature profiles; probe orientation is decided considering the effect of magnetic fields; and a circuit is proposed which will act to filter the effect of RF fluctuations due to inductive coupling the source. After defining the appropriate materials for the probe construction, the electrostatic probe project is presented, together with solutions for probe manipulation and suggestions for data sampling.

Sommario

L'esperimento NIO1 è una sorgente compatta e modulare di ioni negativi costruita presso il Consorzio RFX, Padova, con lo scopo di studiare la configurazione ottimale per una sorgente di ioni negativi del tipo richiesto dall'esperimento di fusione nucleare ITER. In questa prospettiva, una diagnostica completa della sorgente di NIO1 è essenziale. Il presente lavoro di tesi ha lo scopo di sviluppare un sistema di sonde elettrostatiche che misurerà all'interno della sorgente lungo due direzioni ortogonali, fornendo dei profili di densità e temperatura elettronica. Il lavoro inizia con uno studio dei requisiti sul progetto della sonda imposti dalla natura del plasma nella sorgente: la dimensione della sonda è ottimizzata studiando simulazioni di profili di densità e temperatura elettronica; l'orientazione della sonda è decisa considerando l'effetto dei campi magnetici; ed è proposto un circuito che avrà la funzione di filtrare le fluttuazioni RF dovute all'accoppiamento induttivo della sorgente. Dopo aver definito i materiali appropriati alla costruzione della sonda, viene presentato il progetto delle sonde elettrostatiche, insieme alle soluzioni per il loro inserimento e traslazione ed indicazioni per la raccolta dei dati.

Contents

Chapter 1

Introduction

1.1 Energy from Nuclear Fusion

The world's hunger for energy is incessantly increasing. The International Institute for Applied System Analysis (IIASA) has estimated that by the year 2050, the global electricity demand will go up by a factor of 3 and the requirements beyond 2050 go up even higher. Such fast growth in the developing world simply cannot be sustained by the ever-dwindling and environment-degrading reserves of fossil fuels. (In (1)). In this scenario, Fusion Energy plays a key role. In fact, a fusion reaction is about four million times more energetic than a chemical reaction such as the burning of coal, oil or gas.

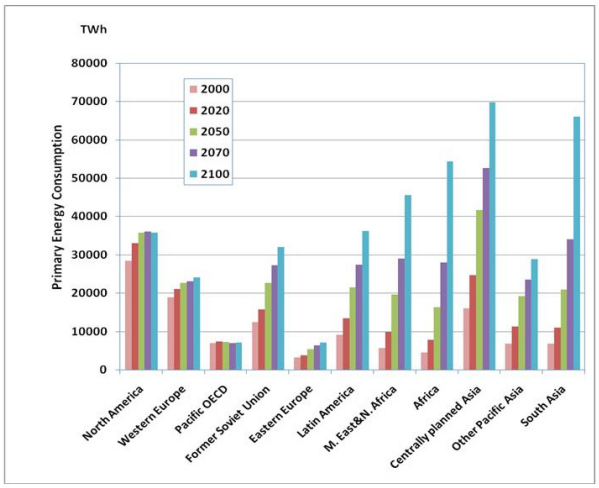

Figure 1.1: Energy demand, from (1)

In a fusion reaction, two light nuclei collide and fuse producing a heavier nucleus and other products. If the sum of the mass of the reactants is more than that of the products, then the reaction gain is positive and the mass excess adds to the kinetic energy of the products. For such a reaction to occur, the colliding nuclei need to have enough kinetic energy to overcome Coulomb repulsion. For instance, at the Sun's core, where hydrogen is burnt to produce helium, the temperature of the gas is 15 million Kelvin.

At such temperatures, matter is ionised in a new state called plasma. In stars, this hot gas of charged particles is confined thanks to gravity, but we cannot exploit this fact on Earth, and in fact fusion researchers have been studying other methods to confine and heat the gas since the 1950s, when experimental research on plasma confinement systems for a prospective reactor started at Kurchatov Institute, Moscow.

Plasmas

Plasma is a state of matter in which a considerable fraction of ionised atoms or molecules is present, together with free electrons. A plasma is characterised by the parameters in Table (1.1). In equilibrium conditions, the plasma would be quasi-neutral, that is $n_i \approx n_e$. The ratio of the charged particle density to the neutral density is denoted as the ionisation degree, $\alpha = n_e/n_n$: if $\alpha \ll 1$, the plasma is weakly ionised, if $\alpha \approx 1$ the plasma is fully ionised. If the

		full variation range
neutral density	n_n	
ion density	n_i	
electron density	n_e	$[10^3 m^{-3} - 10^{33} m^{-3}]$
neutral temperature	T_n	
ion temperature	T_i	
electron temperature	T_e	[1 eV - $10^6 eV$]

Table 1.1: Characteristic plasma parameters

electron and ion temperatures are equal $T_e \approx T_i$, the plasma is a thermal medium and usually is denoted as "hot plasma".

1.1.1 Advantages of Fusion Energy

Widely available fuel: The D-T reaction displayed in Eq. (1.1) has been identified as the process that would give the highest yield and efficiency in a fusion device. In this process, a deuterium and tritium nuclei fuse producing an alpha particle (stable helium nucleus) and a neutron. The reaction has a Q-value (gain due to mass excess) of 17.6 MeV.

$$^2H +^3 H \rightarrow^4 He\ (3.5MeV)\ + n\ (14.1MeV) \tag{1.1}$$

Deuterium can be industrially distilled from water. In every litre of seawater, for example, there are 33 mg of deuterium. Tritium is a fast-decaying isotope which occurs only in trace quantities in nature. It can however be produced in the reactor itself, when neutrons escaping the plasma interact with lithium contained in a special "blanket wall".

$$n +^6 Li \rightarrow^4 He +^3 H +\ 4.8MeV \tag{1.2}$$

$$n +^7 Li \rightarrow^4 He +^3 H + n +\ 2.5MeV \tag{1.3}$$

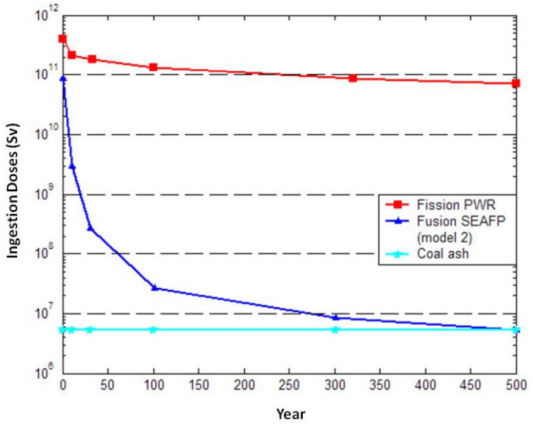

Figure 1.2: Time decay of waste products environmental doses, from (1)

Small fuel feeding: Only a few grams of deuterium and tritium will be necessary to fuel the reactor. To make a comparision, while a 1000MW coal-fired power plant requires 2.7 million tons of coal per year, a future fusion plant will require only 250kg of fuel per year. (source: ITER website)

Innocuous products: Fusion emits no pollution; the major product is helium, a stable, inert, non-toxic gas.

Safety: There is no possibility of a "runaway" situation leading to a nuclear accident like that of Chernobyl; the conditions for fusion are so difficult to be achieved that, should there be any failure in the reactor's control system, the plasma would simply cool down and recombine to a neutral gas. The by-products of fusion are neutrons, which can activate the reactor walls material as is the case with fission reactors. This activation is however weaker for fusion reactors and, as shown in Figure (1.2), the radioactive waste decays on a timescale of only a few hundred years.

1.1.2 The ITER Project

The ITER project started in 1985 and aims to demostrate the technological and scientific feasibility of fusion energy. The reactor is being built in Cadarache (France) under an international cooperation formed by USA, Russia, EU, Japan, China, South Korea and India.

The ITER machine shown in Figure (1.3) is designed to produce a fusion power of 500MW with a 50MW input power, thus becoming the first of all fusion experiments to produce net energy.

Fuel and electricity production

ITER is designed to work with a D-T plasma, exploiting reaction (1.1) to produce energy. If the plasma is externally heated to a temperature of 20keV, the energy of the helium nuclei produced in the reaction is high enough to maintain the fusion temperature of the plasma so external heating systems may be switched off. The turning point is called "burning condition" and its attainement is essential for the industrial feasibility of a fusion plant.

This reaction has a 80% neutronicity (ratio of neutron final energy to Q-value), so the electric energy production envisioned in a future fusion plant will be based on conventional steam turbines: neutrons impact on the external water-containing vessel and heat it via kinetic energy transfer. Future second generation reactors will be based on neutronless reactions like the proton-boron reaction in Eq. (1.4), where the kinetic energy of the products is directly converted into electricity and no radioactive shielding is needed (neutronicity will be 0.1%, from (1)).

$$p + {}^{11}B \rightarrow 3\ {}^{4}He \tag{1.4}$$

Plasma confinement

ITER is based on the 'tokamak' concept of magnetic confinement, in which the plasma is contained in a toroid-shaped vacuum vessel. Strong magnetic fields are used to keep the plasma away from the walls; these are produced by superconducting coils surrounding the vessel, and by an electrical current driven through the plasma. The combination of toroidal and poloidal magnetic fields and centrifugal pressure gradient can effectively act as a so-called 'MHD screw-pinch'.

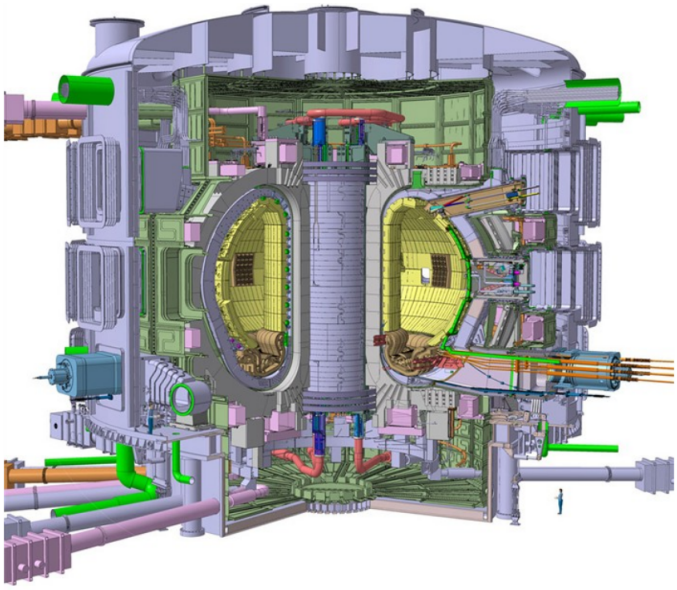

Figure 1.3: Overview of the ITER machine: man in the bottom right corner for size comparision, from (2)

Plasma heating

Three heating mechanisms will work together in ITER:

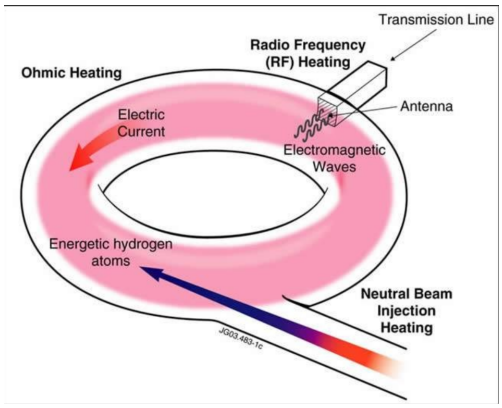

Figure 1.4: ITER heating mechanisms

Ohmic heating: plasma resistivity ρ_{el} (1.5) depends on the collision frequency ν_{coll}.

$$\rho_{el} = \frac{m_e \nu_{coll}}{e^2 n_e} \tag{1.5}$$

In a fully ionised plasma, ν_{coll} decreases with $T_e^{-3/2}$ so ohmic heating is limited to a certain temperature at which equilibrium is reached between input energy and losses.

Neutral Beam Injection heating: NBI heating consists in shooting high energy neutral particles into the plasma. Outside of the tokamak, charged deuterium particles are produced and accelerated to the required energy level. These accelerated ions then pass through an "ion beam neutralizer" and are injected into the tokamak where via collision they transfer their kinetic energy to the plasma increasing its thermal energy. The neutral beam could in principle be created neutralising positive H or D ions, but the neutralisation efficiency for positive ions decreases drastically for energies above 100 keV/nucleon, while keeping at around 60% for negative ions. (3) The beam energy must be considerably higher than the thermal energy of the fusion plasma for the mechanism to be effective; in ITER the beam energy required is 1MeV. The beam neutrality is necessary for it to penetrate the tokamak magnetic field. The structure of an ITER deuterium NBI is shown in Figure (1.5).

RF microwave heating: Ion and electron cyclotron heating methods use resonant radio frequencies waves to deliver into the plasma the additional heat necessary for burning.

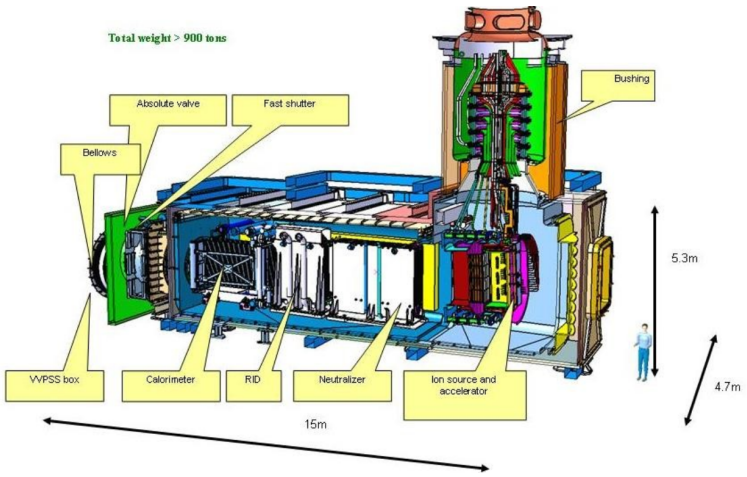

Figure 1.5: ITER Neutral Beam Injector, from (2)

1.2 The NIO1 experiment

The negative ion source NIO1 (Negative Ion Optimisation try 1) is a test facility which came into operation in 2014 at Consorzio RFX, Padua (IT), with the cooperation of INFN-LNL National Laboratory, Legnaro (IT). Its main purpose is to investigate the optimal conditions for a negative source of the type needed for ITER neutral beam injectors. Unlike ITER injectors, NIO1 is characterised by a high modularity which allows relatively rapid and effortless changes

in the experimental setup. NIO1 can operate with various gasses, but at present only hydrogen is being employed.

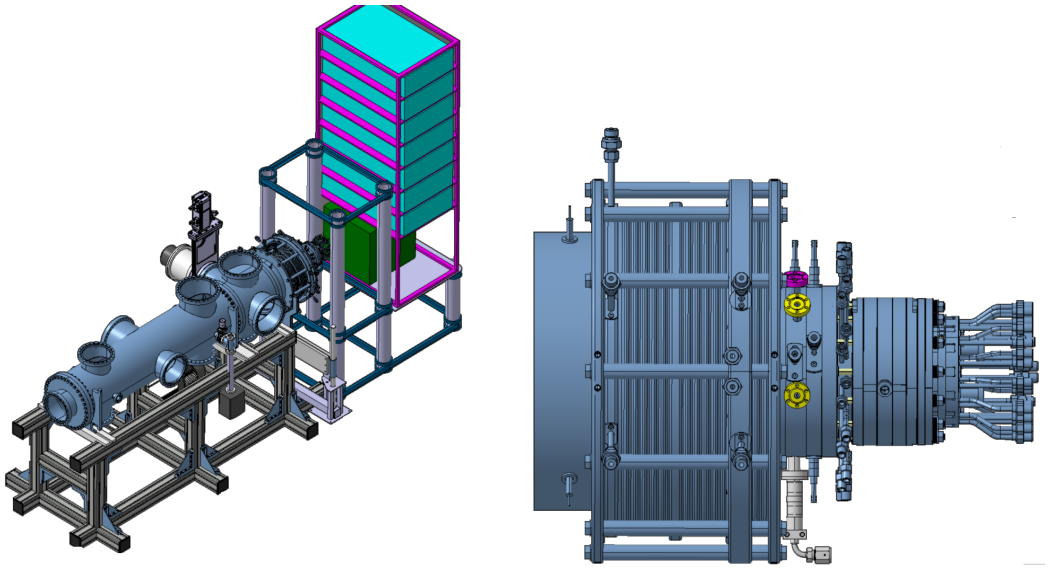

(a) Experimental setup (b) Source and extraction region overview

Figure 1.6: NIO1

1.2.1 Experimental setup

Overviews of the NIO1 setup and source are shown in Figure (1.6a) and (1.6b). The NIO1 structure can be divided in three main parts and is outlined in Figure (1.7):

- Plasma source
- Negative ion extraction and acceleration region
- Beam diagnostic tube

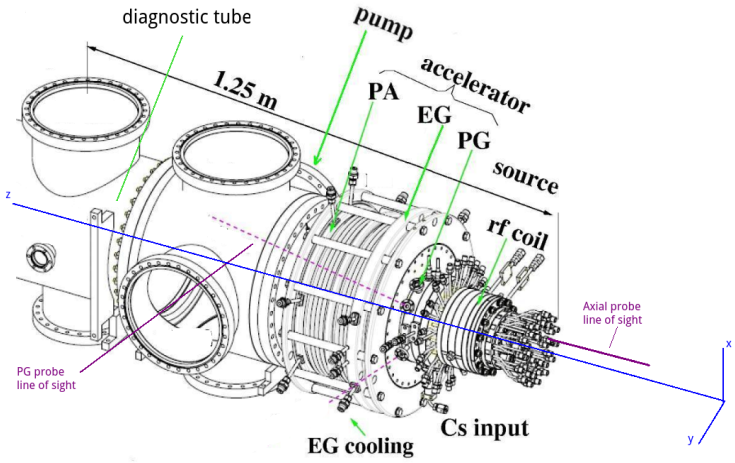

Figure 1.7: Outline of NIO1 structure, from (4)

Plasma source

The source is a 70mm-long cylindric chamber with a 100mm internal radius. A 7-turn coil is wound around the chamber to create plasma by inductive coupling. The RF coupling frequency is (2.0±0.2)MHz and the maximum total power transfer is 2.5kW. In a RF discharge, if the imposed frequency is lower than the electron plasma frequency, $f < \frac{1}{2\pi}\sqrt{\frac{n_e e^2}{\epsilon_0 m_e}}$, then the electrons can follow the oscillation producing ionising collision and, hence, a plasma.

The plasma provided by the NIO1 source is a low temperature, weakly ionised plasma (LTP) in non-thermal conditions, i.e. $T_i \ll T_e$.
An LTP consists largely of neutral gas atoms or molecules and, to a lesser extent, electrons and positive ions. Since the ionisation degree is of order 10^{-4}, we may neglect Coulomb scattering among charged particles and only consider elastic collisions of electrons or ions on neutral particles. Owing to the small mass of the electrons, only a poor energetic contact with the heavy gas particles can be established by elastic collisions. As a consequence, the electrons reach a mean kinetic energy which is much higher than that of the neutral and charged heavy plasma components, and the plasma becomes a non-thermal medium. Typical energies may range in the interval $[0.5eV - 5eV]$ for electrons and $[0.025eV - 0.05eV]$ for heavy particles, which corresponds to 1-2 times the room temperature, [300K-600K] (5) . A more detailed description of the parameters of the source plasma will be given in Section (1.2.2).

Negative ion production

Although negative ions are easier to neutralize, they are also more challenging to create and handle than positive ions. The additional electron that gives the ion its negative charge is only loosely bound, and consequently readily lost.

The production of negative hydrogen ions is driven by *volume* and *surface* phenomena.

- **Volume production:** hydrogen molecules are efficiently vibrationally excited by collisions with high energy electrons ($E_e > 20eV$)

$$H_2 + e_{fast} \rightarrow H_2^* + e_{fast} \tag{1.6}$$

  and negative hydrogen ions are produced by dissociative attachment of low-energy electrons ($E_e < 2eV$) to vibrationally excited molecules.

$$H_2^* + e_{slow} \rightarrow H^- + H^0 \tag{1.7}$$

- **Surface production:** negative hydrogen ions can be produced via collision with caesiated walls; it has been shown that caesium vapour can enhance negative ion production by a factor 3-10 (3). This is due to the fact that ceasium lowers the metal surface work function.

Both mechanisms are actually effective only if a magnetic filter is introduced; negative ions are in fact easily destroyed by collisions with not-slow electrons, so the magnetic filter will act to separate the hotter upstream "driver" region from the cooler "extraction region".

Beam extraction and acceleration

The accelerating column consists of four grids, equally spaced by 14mm, with a 3x3 matrix of apertures for the nine 3.8mm radius beamlets. The total extracted current is 135mA:

- Plasma grid (PG),is the grid facing the plasma and is held at the source voltage (-60kV).
- Extraction grid (EG), is held at a higher potential than the PG (-52kV); the value of the EG potential determines the amount of extracted current.
- Post acceleration grid (PA), held at ground potential; the voltage drop between PG and PA determines the final energy of the beam particles.
- Repeller grid (REP), which can be slightly positively biased (up to 150V) to suppress backstreaming of positive ions.

NIO1 magnetic fields

There are two sources of magnetic field inside NIO1. The major volume contribution is a strong multipole due to the array of permanent magnets installed on the source chamber to provide plasma confinement. The multipole configuration is a "minimum B magnetic bottle" including a rear multipole at the back of the RF source, as shown in Figure (1.8.a).

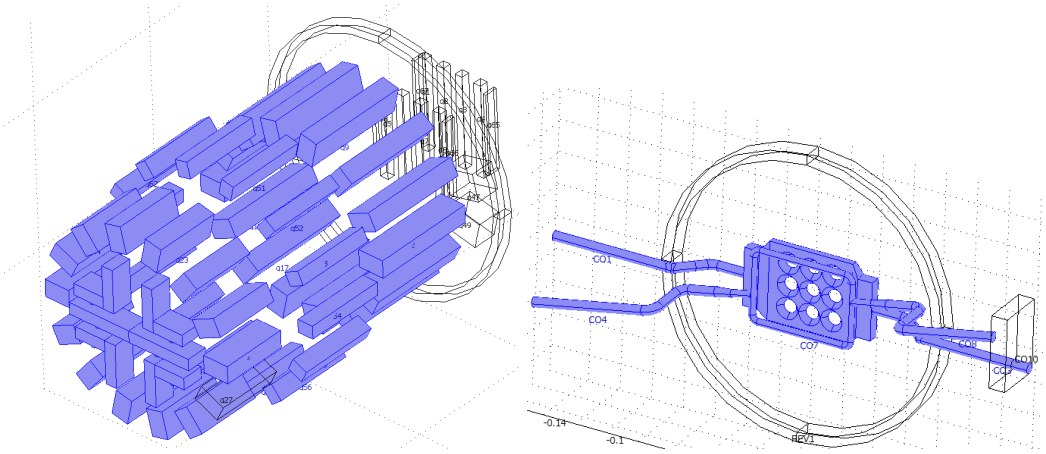

(a) Magnetic multipole (b) PG dipole filter

Figure 1.8: NIO1 magnets

The other contribution is a dipole localised at the Plasma Grid (PG), see Figure (1.8.b), and generated by a current flowing in the PG and tunable to a maximum value of 400A. This dipole field is necessary to prevent the most energetic electrons from diffusing into the extraction region where the production and extraction of negative ions takes place. Both in the present "volume production" and in the soon-to-be-implemented "surface-production" with Caesium, the presence of energetic electrons would lead to stripping and neutralisation processes, competing with the H^- production.

1.2.2 The NIO1 plasma simulation

A model for the NIO1 plasma parameters has been developed by (6) and (7); the model simulates a H_2 discharge taking into account the effect of a confinement multipole magnetic field and a non-uniform deposition of RF power in the driver.

Average dependencies on power and pressure

A power scan (Figure (1.9)) at fixed gas density ($T_{gas} = 400K$, $p_{gas} = 1Pa$) showed that n_e increases linearly with P_{abs}, while the model does not predict a variation of T_e with the absorbed power P_{abs}. The total power transferred to the plasma was changed by varying the current I_{RF} flowing through the coil.

A pressure scan in the range $[0.1Pa - 10Pa]$ with fixed total power deposition, $P_{abs} = 2kW$ was also performed. The results showed that the temperature decreases with increasing pressure (Figure (1.10.b)), whereas the electron density increases but reaches a limiting value at high pressures ($\bar{n_e} \approx 4 \cdot 10^{17} m^3$) because of the high localisation of the electron density under the coil (Figure (1.10.a)).

1.2.3 Source diagnostics

A description of present diagnostics on NIO1 can be found in (8).

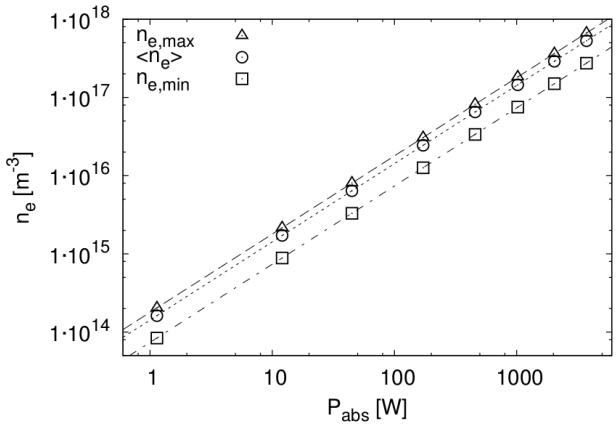

Figure 1.9: n_e as a function of RF power, from simulations

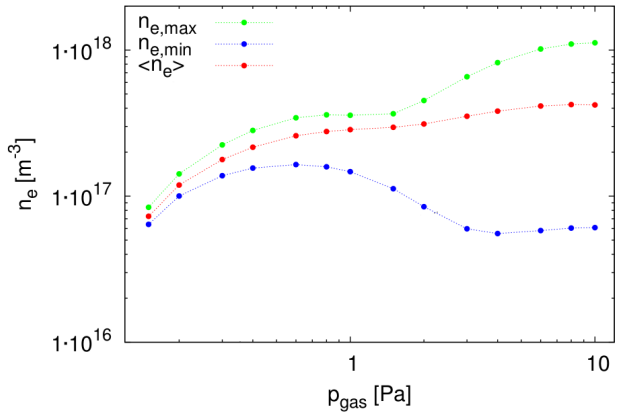

(a) n_e from simulations

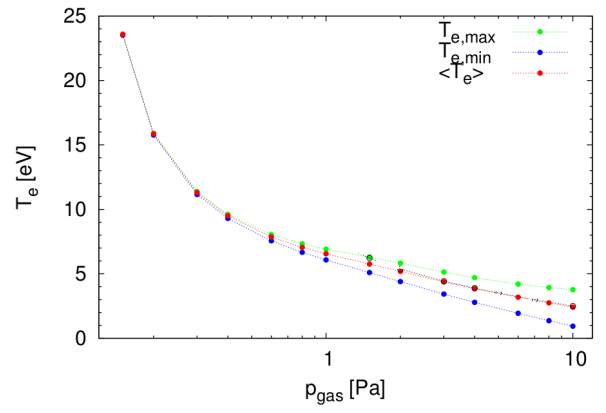

(b) T_e from simulations

Figure 1.10: Simulated plasma parameters as a function of pressure

Plasma Light Detection (PLD) is based on the fast response of a photodiode or photomultiplier. It is useful for detecting the plasma ignition or its switching off, but also for studying fast plasma dynamics.

Source Emission Spectroscopy (SES) features two spectrometers: a low resolution spectrometer which monitors the presence of impurities in the plasma and records the intense and isolated lines of the Balmer series; a high resolution spectrometer is used for solving the rotational and vibrational molecular spectra. The analysis of the spectra gives the electron temperature and the electron, positive and negative ion and caesium densities.

Cavity Ring Down Spectroscopy (CRDS) will soon be installed to provide measurements of the negative ion density inside the source using the photodetachment process; a laser pulse is forced to bounce back and forth between two collinear windows while crossing the medium to be measured. The amount of signal reduction is proportional to the negative ion density.

Laser Absorption Diagnostic (LAD) is being deisgned to allow measuring caesium density inside the plasma source: it will measure the absorption spectrum of a laser tuned to a resonant transition of atomic caesium, without needing a-priori knowledge of the electron density and temperature.

1.2.4 The electrostatic probe project

The aim of this work is to design an electrostatic probe system for the NIO1 source region. This diagnostic will give measurements of electron temperature, ion and electron density, plasma potential, and the data analysis will also enable to reconstruct the electron energy distribution function, EEDF.

The main advantage of this diagnostic is that electrostatic probe measurements are local, unlike spectroscopy measurement which average parameters along their line of view. This enables to obtain spatial but also time resolution, measuring plasma inhomogeneities and fluctuations. The probe "resolving power" is however limited by its dimension and by the characteristics of the plasma it measures. Electrostatic probes are also easy to manufacture.

The available lines of sight for the probes are shown in Figure (1.11): the "axial probe" will be parallel to the chamber axis and will be inserted from the driver rear, the "PG probe" will scan radially parallel to the PG and will be inserted at a distance of 20mm from it.

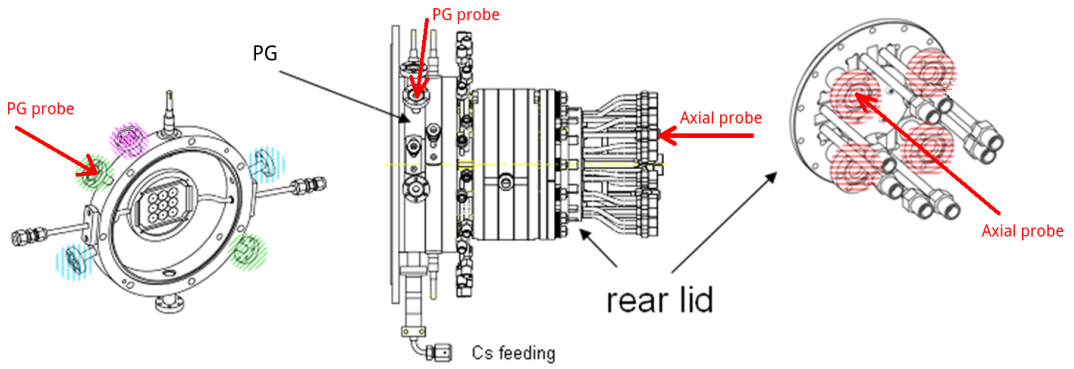

Figure 1.11: Available accesses and lines of sight of the probe system

1.3 Electrostatic probes

Electrostatic probes or Langmuir probes were the first approach to plasma diagnostics, being first used by Langmuir in 1924. Langmuir probes are the diagnostic that can be used

on the widest range of plasma parameters, for densities in the range $[10^6 m^{-3} - 10^{19} m^{-3}]$ and temperatures in the range $[0.1eV - 100eV]$. The working principle of Langmuir probes is rather straightforward: they consist of electrodes inserted in a plasma and polarised at different potentials in order to collect particle fluxes of ions or electrons. The current voltage (I-V) characteristic analysis allows to obtain plasma parameters such as T_e, n_i, n_e and the electron energy distribution function $EEDF$. The difficulty in performing such measurements is linked to their being local, therefore it is essential to establish an understanding of how the probe perturbs the plasma around it, and how the measured parameters are linked to the ones of the unperturbed plasma.

1.3.1 Debye sheath and pre-sheath

When a conductive object is inserted in a plasma, a layer forms at the interface between the plasma and the solid surface: this layer is called Debye sheath and its length is denoted as λ_D.

$$\lambda_D = \sqrt{\frac{\epsilon_0 k_B T_e}{n_e e^2}} \tag{1.8}$$

The pre-sheath extends further in the plasma, and depending on the object geometry, it can be of order 10 Debye lengths thick.

The existence of the sheath is linked to the nature of the plasma. The electron mean velocity v_e is always much higher than the ion's v_i owing to the mass difference as shown in Eq. (1.9).

$$v_e = \sqrt{\frac{8k_B T_e}{\pi m_e}} \gg v_i = \sqrt{\frac{3k_B T_i}{m_i}} \tag{1.9}$$

Thus, since the particle flux $\Gamma = 1/4nv$ as calculated from kinetic theory is proportional to the density-velocity product, the electron flux to the object will be much greater than the ion's, the object collects the electrons charging negatively and eventually a positive charge layer with a strong electric field forms around it. The pre-sheath forms to smoothly join the Debye sheath and the unperturbed plasma: this is a layer of non-equilibrium quasi-neutral plasma, that is, there exists a small electric field of order $k_B T_e/2$.

1.3.2 Probe I -V characteristic

The current-voltage characteristic of an ideal sigle Langmuir probe is shown in Figure (1.12).

If the electrode is insulated (floating electrode) it will charge up negatively attracting positive ions until it reaches the so-called floating potential V_f at which the impinging electron and ion fluxes are equal and the net current is zero. By biasing the probe to a potential $V > V_f$, one reaches the unperturbed plasma potential V_p, at which the probe collects the free electron current I_e. In the case of a planar probe, if the voltage is further increased, the electron current saturates since all impinging electrons are collected; the ion current I_i decreases because of the ion repulsion, but is still negligible compared to the electron current. Reducing the probe potential, $V < V_f$, a larger fraction of electrons will be reflected by the negative probe, until eventually only the ion current will be collected, reaching saturation.

As it is evident from Figure (1.12), the electron current does not saturate for cylindrical and spherical probes: this is because the thickness of the sheath is not fixed, but grows with voltage at high biasing potentials. For this reason, planar probes characteristics are easier to be interpreted.

The saturation values depend on the probe area and the type of plasma considered but generally it is found that the ion saturation current for a planar probe, Eq. (1.10), is

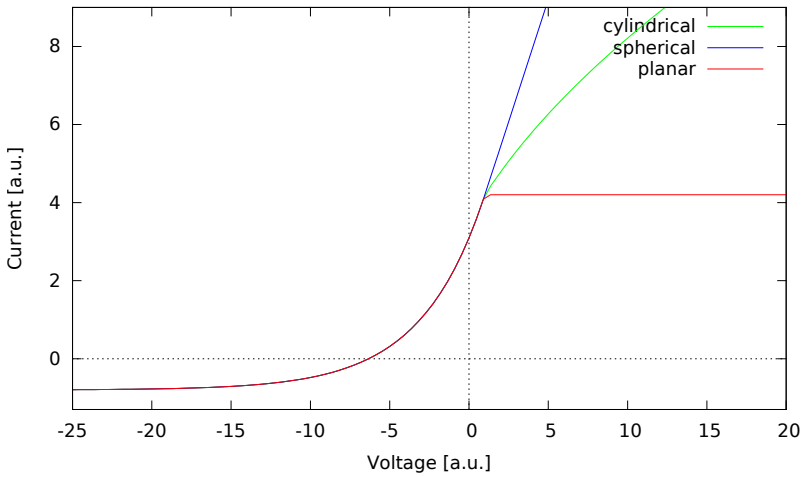

Figure 1.12: I - V probe characteristic

typically of order 100mA whereas the electron saturation current, Eq. (1.11), can be in the range 1-10A. A in the formulae denotes the probe area.

$$I_+ = -\frac{1}{2} e n_e A \sqrt{\frac{k_B T_e}{m_i}} \tag{1.10}$$

$$I_- = \frac{1}{4} e n_e A \sqrt{\frac{8 k_B T_e}{\pi m_e}} \tag{1.11}$$

In the transition region the electron current is given by Eq. (1.12).

$$I(V) = I_+ + I_- \exp\left(\frac{e(V - V_p)}{k_B T_e}\right) \tag{1.12}$$

Plasma parameters can be obtained from the I-V characteristic analysis. The exponential in the transition region can be fitted to obtain the electron temperature; from the ion and electron saturation currents we can afterwards derive the plasma density. The "knee" of the curve corresponds to the plasma potential. The floating potential corresponds to the intersection of the curve with the x-axis. The electron distribution function is proportional to the second derivative of the characteristic.

$$f_{MB}(E) \propto \frac{\delta^2 I}{\delta V^2} \tag{1.13}$$

The characteristic shown in Figure (1.12) is obtained in the ideal collisionless case, that is, when ions and electrons arrive at the probe by free flight. Probe behaviour differs significantly between situations where collisions of electrons on neutral or charged particles can be ignored and those where they cannot. The effect of collisions is generally to reduce the current to the probe because of the necessity of particles to diffuse up to the electrode, rather than arriving by free flight.

Chapter 2

Crucial parameters in probe dimensioning

In designing the probe it is first of all necessary to carefully consider the characteristic of the expected plasma, estimating orders of magnitude, variation ranges and spatial gradients of the parameters of interest, namely the electron density n_e and the electron temperature T_e.

NIO1 can operate at a pressure ranging from 0.1Pa to 10Pa, with an RF power transfer P_{abs} up to 2.5kW; therefore the probe is required to work in a wide parameter range.

In my analysis I will focus on the plasma contained in the driver and extraction region of NIO1, in particular I will study the dependencies of parameters along the available lines of view for the probes.

In order to make the future data analysis easier, important parameters in dimensioning the probe are the Debye length, λ_D and the mean free path, l: they determine the collisional or non-collisional nature of the sheath facing the probe, the extent of the plasma perturbation and the actual geometry of the sheath.

2.1 Debye length

The sheath facing the probe has a thickness of order of ten times the Debye length defined in Eq.(1.8).

Figure (2.1) shows λ_D as a function of pressure, which I calculated using the simulated average values for T_e and n_e. As can be seen, λ_D ranges from $[10^{-5}m - 10^{-4}m]$ for pressures in the range [0.1Pa - 10Pa], as shown in Table (2.1).

Given that P_{abs} is independent of T_e and grows linearly with n_e, the Debye length depends only weakly on the power transfer: $\lambda_D \propto \sqrt{1/n_e}$. The total power transfer will be varied in the range [300 W : 2.5 kW], not wide enough to make the Debye length change in order of magnitude.

	p_{gas} [Pa]	n_e [m^{-3}]	T_e [eV]	λ_D [m]
low pressure regime	0.1	$7 \cdot 10^{16}$	25	$1.4 \cdot 10^{-4}$
intermediate pressure regime	1	$3 \cdot 10^{17}$	6	$3.3 \cdot 10^{-5}$
high pressure regime	10	$4 \cdot 10^{17}$	2.5	$1.9 \cdot 10^{-5}$

Table 2.1: Debye length

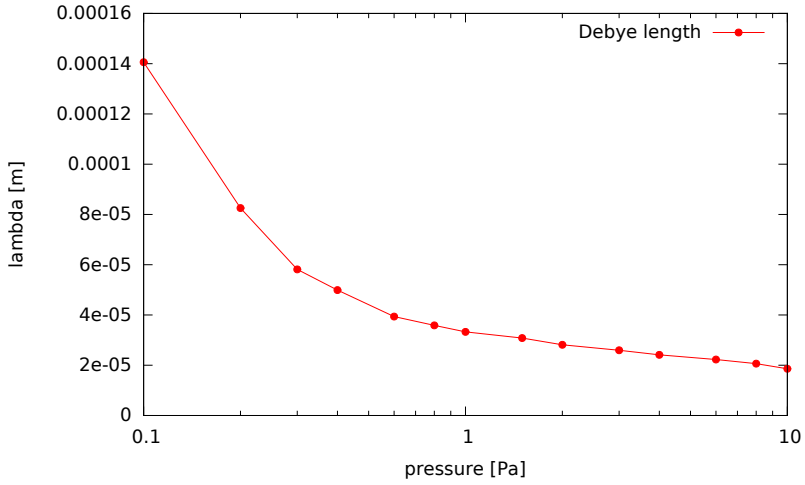

Figure 2.1: Debye length as a function of pressure

2.2 Mean free path

The relevant colliding particles are electrons and Hydrogen ions H^+ and H_2^+ and the dominant type of collision is the elastic scattering on neutrals. The mean free path l for elastic collisions is defined as follows.

$$l = \frac{1}{n_n \sigma_{el}} \tag{2.1}$$

where n_n is the density of neutrals and σ_{el} is the cross section for elastic collision on Hydrogen molecules.

I extracted cross section values at the expected kinetic energy as shown in Table (2.2) from the articles (9) for the electrons, and (10) for the positive ions. Anelastic collisions will also be present, but the corresponding cross sections are typically 2 orders of magnitude below the elactic scattering value (from data collected in (10)).

	Kinetic Energy [eV]	σ_{el} [m^{-2}]
e^-	1 - 10	10^{-19}
H^+	10^{-2}	10^{-18}
H_2^+	10^{-2}	10^{-21}

Table 2.2: Elastic cross sections

I calculated the mean free path shown in Table (2.3) in the case of low, intermediate and high pressure gas, for a neutral temperature of 400K.

p_{gas} [Pa]	n_n [m^{-3}]	l [m] for e^-	l [m] for H^+	l [m] for H_2^+
0.1	$1.8 \cdot 10^{19}$	$5.5 \cdot 10^{-1}$	$5.5 \cdot 10^{-2}$	55
1	$1.8 \cdot 10^{20}$	$5.5 \cdot 10^{-2}$	$5.5 \cdot 10^{-3}$	5.5
10	$1.8 \cdot 10^{21}$	$5.5 \cdot 10^{-3}$	$5.5 \cdot 10^{-4}$	$5.5 \cdot 10^{-1}$

Table 2.3: Mean free path

2.3 Effect of collisions and plasma perturbation

Comparing the sheath thickness $10\lambda_D$ to the mean free path I verified that in all situations the sheath can be considered collisionless.

p_{gas} [Pa]	$10\lambda_D/l$ for e^-	$10\lambda_D/l$ for H^+	$10\lambda_D/l$ for H_2^+
0.1	$2.6 \cdot 10^{-3}$	$2.6 \cdot 10^{-2}$	$2.6 \cdot 10^{-5}$
1	$6.0 \cdot 10^{-3}$	$6.0 \cdot 10^{-2}$	$6.0 \cdot 10^{-5}$
10	$3.4 \cdot 10^{-2}$	$3.4 \cdot 10^{-1}$	$3.4 \cdot 10^{-4}$

Table 2.4: Sheath thickness to mean free path

A probe perturbation on plasma parameters is weak as long as the sheath thickness is much shorter than the characteristic probe dimension, a. If the sheath is comparable to the probe in size, then the planar approximation is no longer applicable.

$$10\lambda_D \ll a \tag{2.2}$$

From these considerations I concluded that, in absence of any other effects, an ideal, collisionless, planar probe characteristic is obtainable for,

$$1\ mm < a < 10\ mm \tag{2.3}$$

The expectable ion and electron saturation currents are therefore in the range:

$$0.8\ mA < I_+ < 155\ mA \tag{2.4}$$

$$29.5\ mA < I_- < 5.3\ A \tag{2.5}$$

where the lower value is for a smaller probe in a low-pressure plasma, and the upper is for a larger probe in a high-pressure plasma. These values of current are relatively easy to measure and a refined amplifier setup is not needed. Electrostatic probe currents typically range between 100 mA - 10 A; so choosing $a = 5$ mm leads to,

$$22\ mA < I_+ < 39\ mA \qquad 0.7\ A < I_- < 1.3\ A \tag{2.6}$$

2.4 Probe resolution

An important constraint on the probe dimension is determined by the spatial gradients of the parameters of interest. A probe which is too large may in fact average the gradients and give a measurement which is no longer local.

I analised the radial and axial profiles of density and temperature for both intermediate and high pressure regimes to set a limit on probe dimensions.

2.4.1 Axial and radial profiles

Using the code developed by (7), I obtained a profile of the electron temperature and plasma density for a total power transfer of 1kW and pressures of 1Pa and 10Pa.

As can be seen from Fig.(1.10.b) and Fig.(1.10.a) at very low pressures the parameters display a very weak variation in the volume. The profiles obtained are referred to the available lines of sight for the probes previously discussed. The axis sistem is that shown

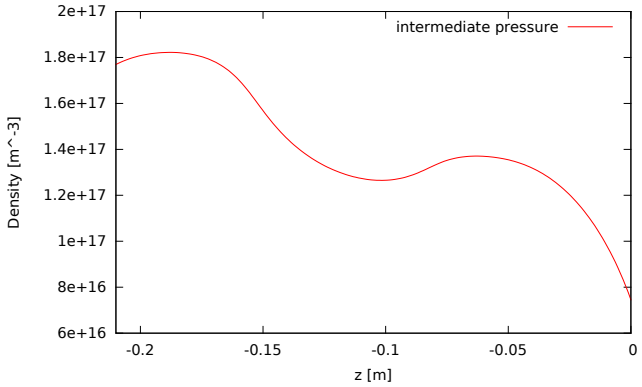

(a) n_e along z, 1Pa

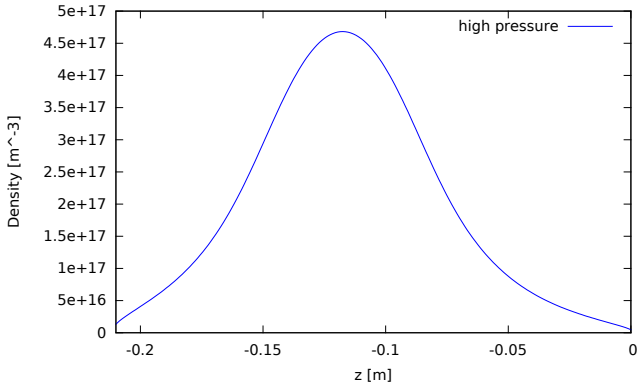

(b) n_e along z, 10Pa

Figure 2.2: Plasma density axial profile at different pressures

in Figure (1.7): the z-axis is along the chamber axis, z=0m corresponds to the PG, while z=-0.21m is the driver rear; while the x-axis is in the vertical direction.

Figures (2.2.a) and (2.2.b) show that the electron density profile at lower pressures has a peak in the back of the driver, where the effect of multipole confinement is stronger, while it becomes steeper in the coil region ($-0.15 < z < -0.08$) at higher pressures. This is the reason why the electron density is lower at the plasma grid in the case of higher pressure, as can be seen in Figure (2.3.a) and (2.3.b).

The electron temperature axial profiles (2.4.a) and (2.4.b) are less steep but display a maximum along the axial direction corresponding to the coil region; this might mean that the electron temperature is not really independent of the absorbed power. Both radial temperature profiles (2.5.a) and (2.5.b) and density radial profiles decrease along the radius as an effect of magnetic confinement.

2.4.2 Signal averaging limit

In order to establish a quantitative understanding of the averaging effect, I defined a "relative error" ϵ_n and ϵ_T with respect to the local measurement along the direction examined. The profiles simulated in Section (2.4.1) are discretised in a spatial step of 1mm which is also the minimum probe dimension that can be analysed.

For every position x^j I considered a probe of dimension a centered in x^j and computed the ratios here defined as relative errors:

$$\epsilon_n = \frac{\Delta n_e}{n_e^j}; \qquad \epsilon_T = \frac{\Delta T_e}{T_e^j} \tag{2.7}$$

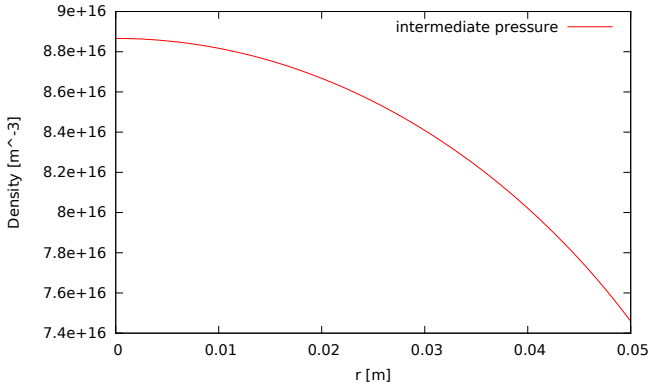

(a) n_e along r, 1Pa

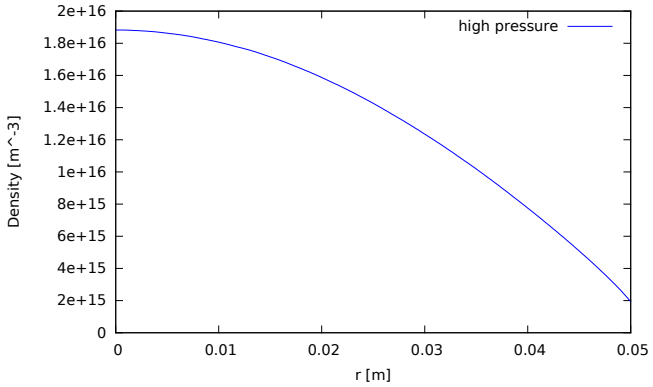

(b) n_e along r, 10Pa

Figure 2.3: Plasma density radial profile at different pressures

where T_e^j and n_e^j are the parameters simulated in x^j, that is, the desirable local measurement; ΔT_e and Δn_e represent the difference between the maximum and minimum simulated values lying within the probe sampling interval

$$[x^j - a/2 \ : \ x^j + a/2] \tag{2.8}$$

The probe dimension was varied from 1mm to 10mm.

The main effect of averaging in seen for the plasma density; ϵ_T is negligible for both directions. Figure (2.8) pictures ϵ_n for axial measurements: this parameter is the one exhibiting the steepest gradients and therefore the most sensitive to averaging; It can be seen that in order to have $\Delta n_e/n_e < 20\%$ also at higher pressures it is necessary to choose a probe whose dimension is not greater than 5mm. Besides, it not convenient to reduce the probe dimension for the sake of locality, for Langmuir probe data are often affected by noise which translates into an error of 10-20% of the value measured.

2.4.3 Array spacing limit

On the other hand, an analogous calculation can be performed in order to obtain the optimal spacing of probes in an array. If the probes are placed too close to each other, the existing difference in the values may be blurred by the noise, so making the array setup useless.

I defined a "relative variation" v_n as the absolute relative increment of parameters for subsequent points on an array with spacing d.

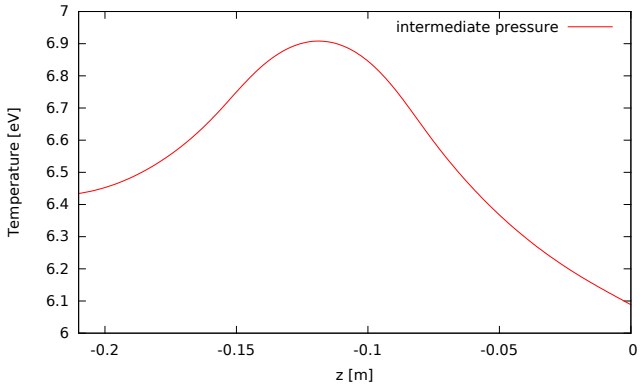

(a) T_e along z, 1Pa

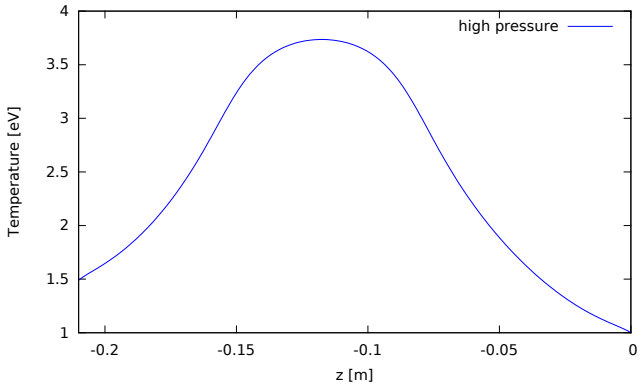

(b) T_e along z, 10Pa

Figure 2.4: Electron temperature axial profile at different pressures

$$v_n = \frac{|n_e^j - n_e^{j+d}|}{n_e^j} \tag{2.9}$$

where n_e^j is the value simulated in x^j and n_e^{j+d} is the value simulated in (x^j + d). The array spacing was varied from 1mm to 50mm. I only studied the relative variation of density along the axial direction (Fig. (2.10)). Owing to mechanical constraints later discussed (see Chapter 4, Probe design) it is not possible to design an array of probes to be inserted parallel to the plasma grid.

A suitable spacing is d=15mm: in the high pressure regime, a wider spacing would result in large relative increments so, rather than drawing a profile along the array, one would obtain independent measurements. On the other hand, at a lower pressure a spacing which is equal to or shorter than 10mm shows a relative increment of up to 10%; this would make the array structure ineffective because, if we take account of a 5% averaging for a=5mm, the two measurements might not be significanly different from each other.

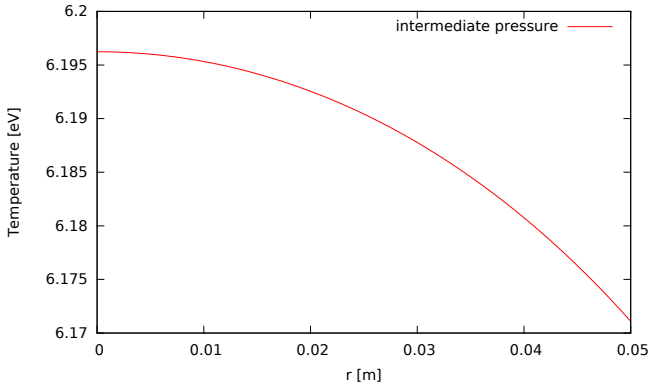

(a) T_e along r, 1Pa

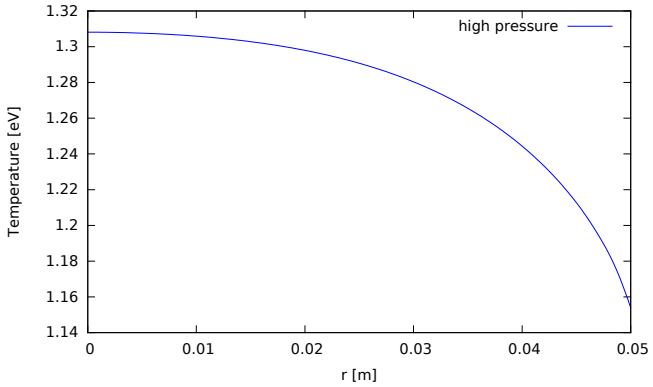

(b) T_e along r, 10Pa

Figure 2.5: Electron temperature radial profile at different pressures

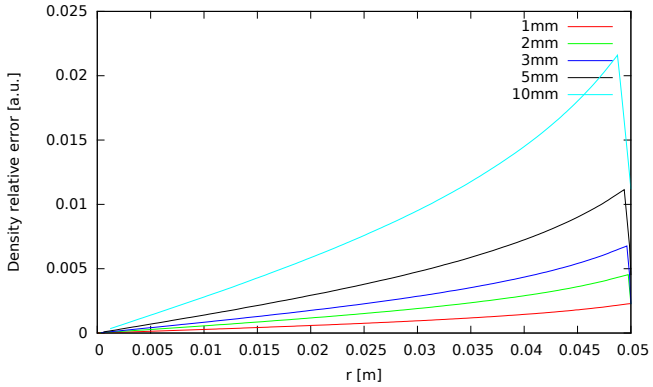

(a) ϵ_n along r, 1Pa

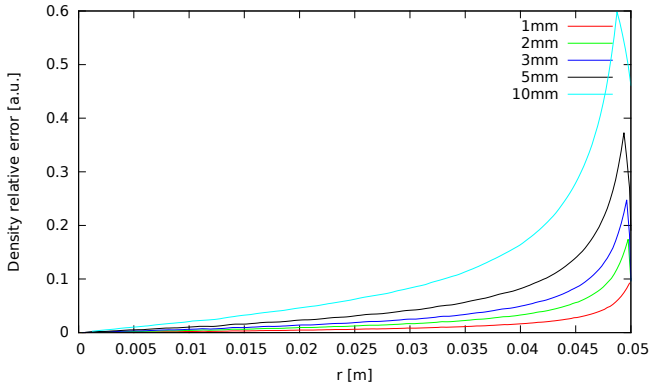

(b) ϵ_n along r, 10Pa

Figure 2.6: Plasma density relative error: radial profile at different pressures

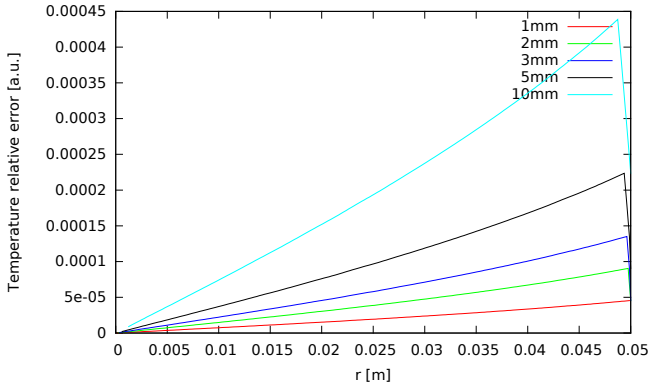

(a) ϵ_T along r, 1Pa

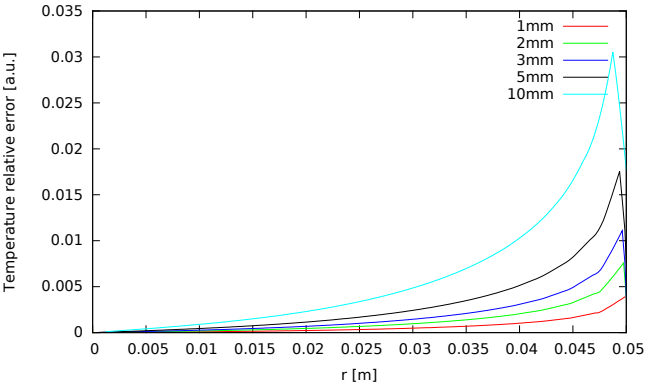

(b) ϵ_T along r, 10Pa

Figure 2.7: Electron temperature relative error: radial profile at different pressures

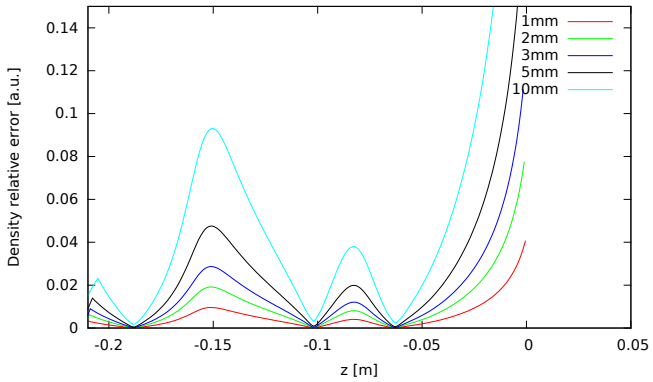

(a) ϵ_n along z, 1Pa

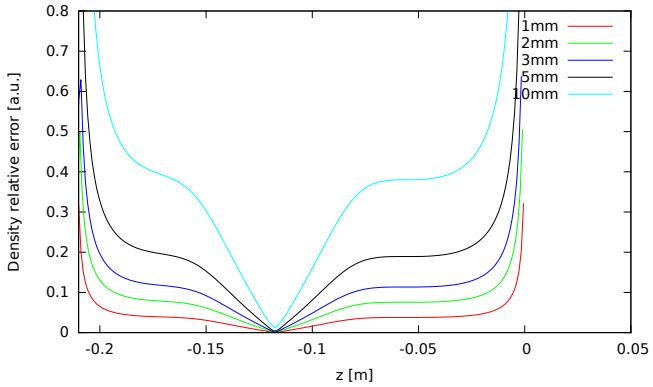

(b) ϵ_n along z, 10Pa

Figure 2.8: Plasma density relative error: axial profile at different pressures

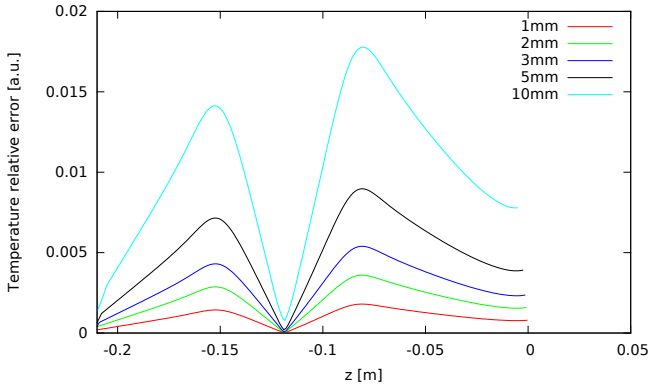

(a) ϵ_T along z, 1Pa

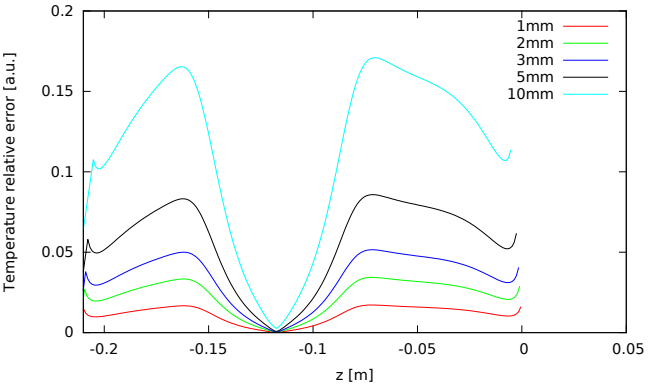

(b) ϵ_T along z, 10Pa

Figure 2.9: Electron temperature relative error: axial profile at different pressures

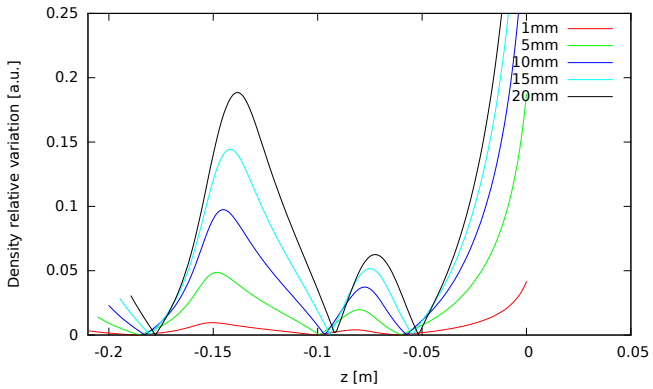

(a) v_n along z, 1Pa

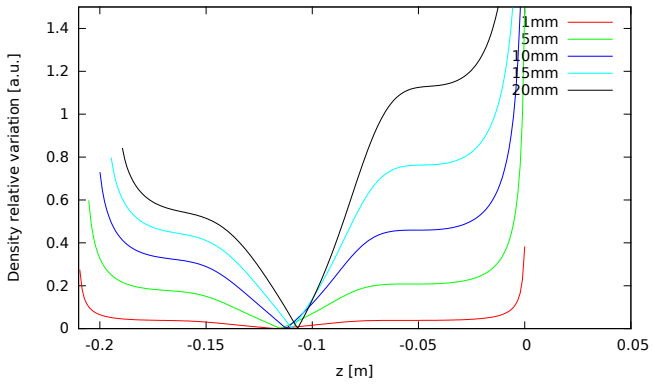

(b) v_n along z, 10Pa

Figure 2.10: Plasma density relative variation: axial profile at different pressures

Chapter 3

Relevant experimental conditions

3.1 Magnetic field effect

The plasma inside NIO1 is magnetised. This fact must be considered in designing the probe geometry, dimension and orientation.

3.1.1 Probes in a magnetic field

The main effect of magnetic fields is to induce charged particles to orbit around the field lines in helical orbits whose characteristic radius is the Larmor radius, R.

$$R = \frac{mv_\perp}{eB} = \frac{\sqrt{2mk_BT}}{eB} \tag{3.1}$$

The effect of magnetic fields on the probe characteristic is generally a reduction of the electron saturation currents.

This fact occurs because the mean free path of charged particles orthogonally to the field lines is no longer l (see eqn.(2.1) on pg. 14), but rather R. In these conditions a collisionless treatment is no longer applicable and one must take account of anisotropic diffusion coefficients: $D_\parallel$ and $D_\perp$.

Particle motion along the field lines is unaffected,

$$D_\parallel = D_0 \tag{3.2}$$

whereas orthogonal diffusion is reduced to,

$$D_\perp = D_0 \left(1 + \left(\frac{\omega_c}{\nu_c}\right)^2\right)^{-1} \tag{3.3}$$

where D_0 is the ambipolar diffusion coefficient in the absence of magnetic fields, $\omega_c = eB/m$ is the particle gyrofrequency and ν_c denotes the collision frequency.

When the plasma around a probe is magnetised, particle collection does not take place in an ideal electrostatic pre-sheath, but we may define a flux tube as the set of all magnetic field lines which cross the probe surface. As parallel diffusion is much faster than orthogonal diffusion, the probe will collect current mainly from this flux tube, eventually depleting it; current collection can however continue either by parallel transport from further regions, or by cross field transport. In the first case, the particles reaching the

electrode come from regions further in the plasma, and have therefore lost part of their energy via collisions; in the second case, orthogonal transport is generated by collisions and in this direction the mean free path is the Larmor radius.

The overall effect is a reduction in the electron current caused by collisions in the flux tube which may scatter particles out of the flux tube; ions are in fact massive and their deflection via scattering is reduced.

The influence of magnetic field is determined by the a/R ratio of the probe dimension to the Larmor radius. If the Larmor radius is large compared to the probe dimension, then orthogonal transport is an effective mechanism for replenishing the flux tube and the electron current reduction does not take place.

$$\frac{a}{R} = \frac{aeB}{\sqrt{2m_e k_B T_e}} \propto B\ {T_e}^{-1/2} \ll 1 \tag{3.4}$$

If on the contrary $a/R \gg 1$, particles can be collected only parallel to the magnetic field and the probe, regardless of its geometry, behaves as a planar probe with a collecting area equal to the probe cross section along the field lines.

The intermediate situation is not analitically solvable. As a general rule, it is preferable to mount the electrodes with their surface orthogonal to the field direction.

3.1.2 Magnetic field profile

The graphs (Fig. 3.1) and (Fig. 3.2) show the confining multipole field profile for the two available lines of sight for the probe as prievously indicated in Figure (1.11).

3.1.3 Larmor radius and probe dimension

Considering an average magnetic field of order $B \sim 10mT$, an ion temperature $T_i = 400K$ and an electron temperature $T_e \sim 10eV$, we find that both ions and electrons are magnetised in NIO1.

$$R_e = \frac{\sqrt{2m_e k_B T_e}}{eB} \sim 1mm \tag{3.5}$$

$$R_i = \frac{\sqrt{2m_i k_B T_i}}{eB} \sim 3mm \tag{3.6}$$

Nonetheless, the effect of magnetisation is more evident for electrons.

I calculated the a/R ratio profile taking into account the probe orientation, so separately considering each component of the magnetic field. I considered the regimes of low (0.1 Pa) and high pressure (10 Pa): at low pressure, T_e is nearly uniform in the source (7), and at high pressure the temperature does not vary by order of magnitude along the directions considered for the probes, so the a/R profile does not change considerably if calculated with the average temperature.

The ratios were calculated for a probe dimension of a=5mm.

Axial probe

Figures (3.3) and (3.4) show the directional a/R ratio calculated at low and high pressure for the axial line of sight. The field considered is the total field given by the superposition of the confinement multipole and PG dipole filter; the PG filter field is actually everywhere negligible and gives only a small contribution close to the grid. The profile can be divided in three regions:

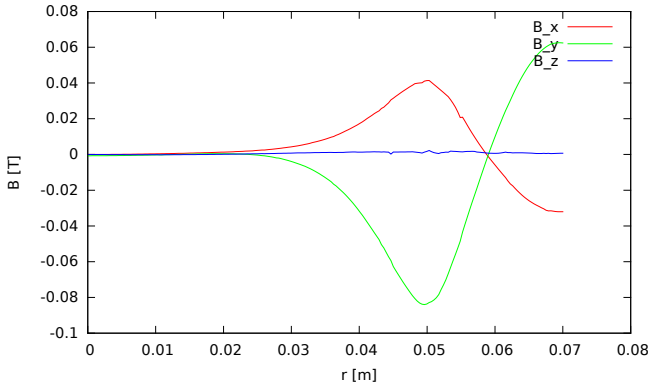

(a) B: Plasma Grid radial profile

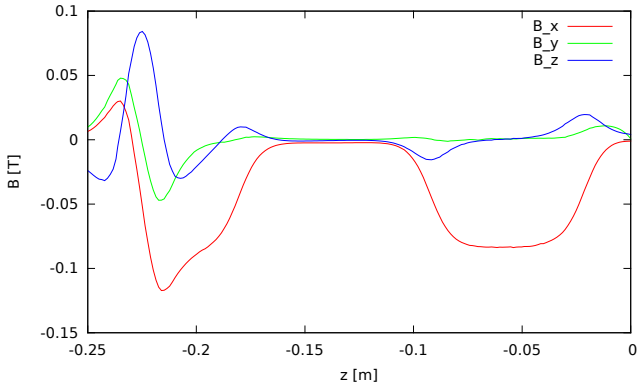

(b) B: axial profile

Figure 3.1: Multipole magnetic field profile

- $-0.25m < z < -0.15m$, rear multipole: in this region the a/R ratio is high for all directions.
- $-0.15m < z < -0.08m$, coil region: in this region the magnetic field effect is weak for all directions.
- $-0.08m < z < 0.0m$, is the expansion region: the ruling effect is along the x-direction.

The effect of the magnetic field is not easily quantifiable in the first region, however, this is not the most interesting region for the axial probe measurements; the aim of the NIO1 experiment is in fact that of optimising the negative ion extraction in the source, so the Langmuir probe measurements will be mostly performed in the region close to the PG.

For this reason, the optimal orientation for the electrodes is with their axis parallel to the x-axis.

PG probe

Figures (3.5) and (3.6) show the directional a/R ratio calculated at low and high pressure for the line of sight parallel to the PG at z=-20mm. The field considered is the total field, sum of PG dipole filter and confining multipole fields; the PG dipole filter gives a small contribution near the axis, but does not considerably change the a/R ratio.

In the two cases examined the a/R ratio for the z-component of the magnetic field is less than unity, so the best orientation of the PG electrode is with its axis parallel to the z-axis.

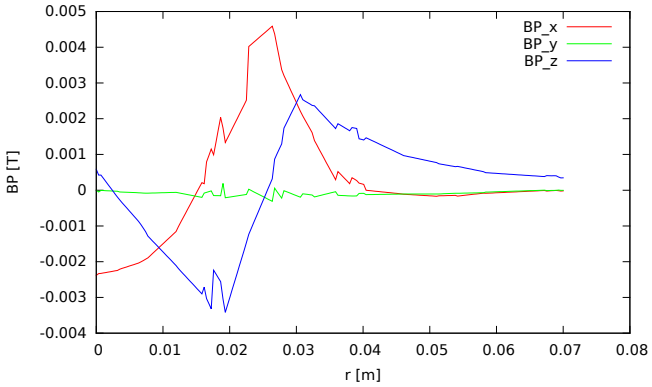

(a) B^{PG}: Plasma Grid radial profile

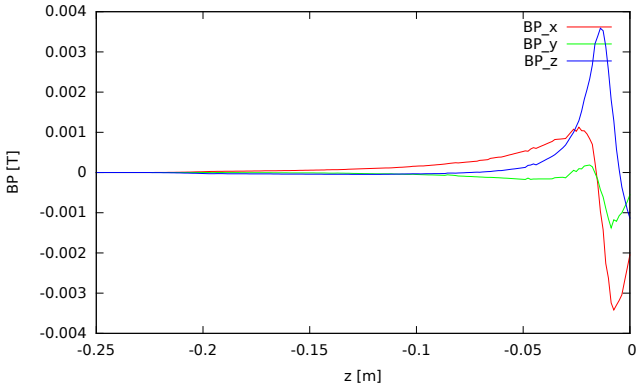

(b) B^{PG}: axial profile

Figure 3.2: PG dipole filter field profile

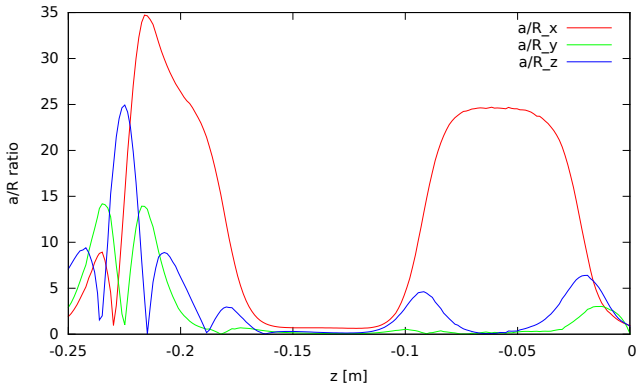

Figure 3.3: a/R ratio for the axial probe: low pressure, total field

3.2 RF coupling effect

The NIO1 source is an inductively coupled plasma source operating at a frequency of (2.0 ± 0.2)MHz with a total power transfer up to 2.5kW. An RF oscillating potential can considerably interfere with the Langmuir probe characteristic. The RF potential appears in the sheath and causes the sheath potential V_S to oscillate in time.

$$V_S(t) = V_S^{DC} + V_{RF}(t) \tag{3.7}$$

An instantaneous I-V measurement would therefore show a horizontal drift of the char-

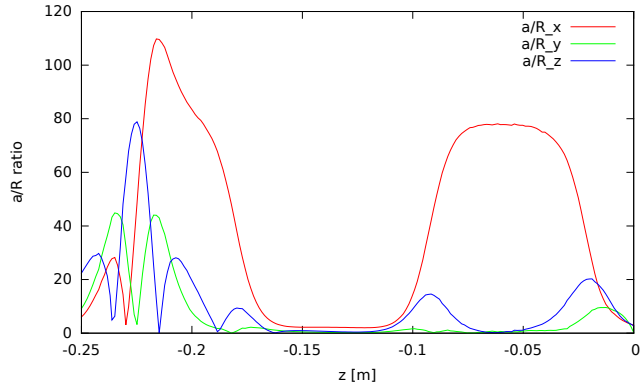

Figure 3.4: a/R ratio for the axial probe: high pressure, total field

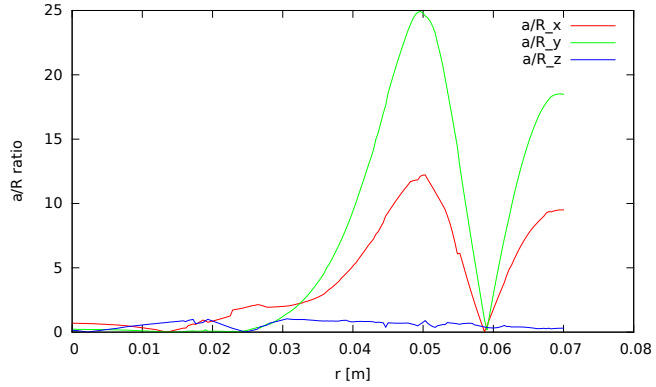

Figure 3.5: a/R ratio for the PG probe: low pressure, total field

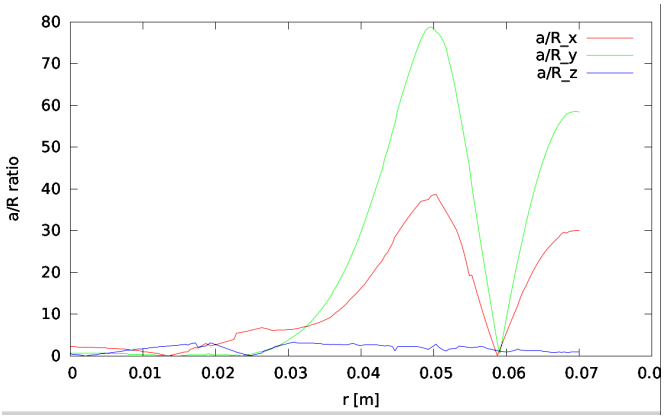

Figure 3.6: a/R ratio for the PG probe: high pressure, total field

acteristic, arising from the additive nature of the perturbation, $V_{RF}(t)$.

$$V_{RF}(t) = Asin(2\pi ft) \tag{3.8}$$

where A is the amplitude of the oscillation.

If the probe is biased at a potential V_B, the current measured will instantly correspond to the DC current at a potential V.

$$V = V_B + V_{RF}(t) \tag{3.9}$$

As can be seen from Figure (3.7), if the sampling frequency is lower than the RF frequency, the data collected is an average measurement between the two extremes of the oscillation. Owing to the non-linearity of the characteristic, the averaged measurement does not coincide with the DC measurement. The knee gets rounded and a true measurement of V_P is impossible. The steep of the curve in the transition region is lowered, and T_e is overestimated.

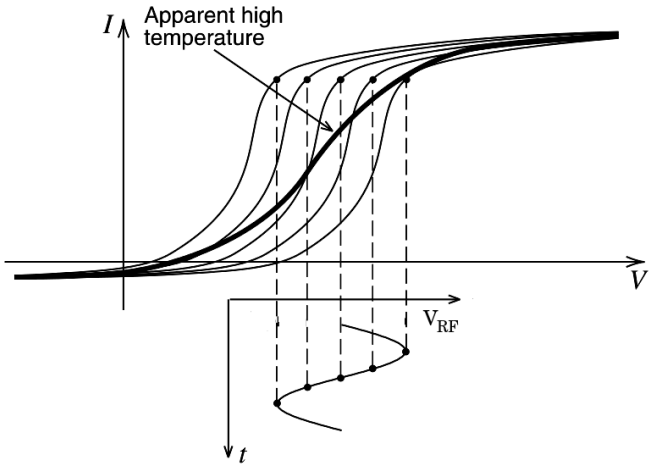

Figure 3.7: Averaging effect of RF perturbation of probe characteristic, taken from (11)

The distortion of the characteristic grows with A as is shown in Figure (3.8). Since the power transfer to the plasma is not uniform in the NIO1 source (6), the distortion effect will be heightened in the region of the coil, that is for $-0.15 < z < -0.08$.

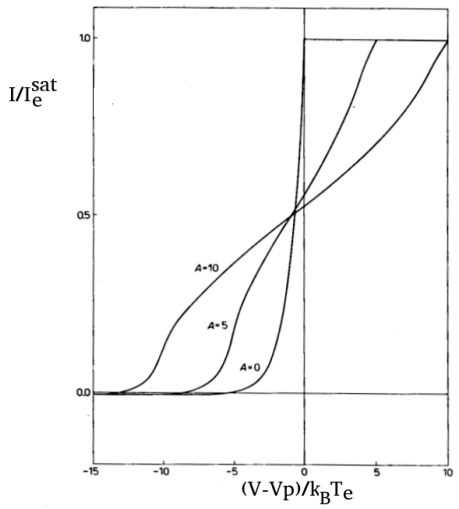

Figure 3.8: Distortion effect of RF perturbation of probe characteristic, taken from (12)

3.2.1 RF compensation

The RF fluctuations can be actively or passively compensated to reobtain a DC characteristic. It is not feasible to actively follow the oscillations charging the probe at the same frequency as the plasma source, because the phase of the perturbation is unknown.

It is as well not feasible to add a floating electrode and feed the signal as an additive perturbation on the probe signal as done in (13) and (14): such a reference electrode would be too large to fit into the access. The viable solution is to insert an anti-resonant LC circuit that acts as a passive band-cut filter as done in (15).

Probe circuit

Figure (3.9) is a schematic view of the probe circuit. V_s is the sheath fluctuating potential, V_P is the plasma potential and V_B is the tunable biasing probe potential. C_{s1} and C_{s2} are stray capacitances introduced by the cables. $R_L \sim 1k\Omega$ is a load resistance that needs to be large in order to minimise the disturbance on the electrode. Z_{sh} is equivalent impedance of the sheath, which is characterised by a sheath resistance R_{sh} and a sheath capacitance C_{sh}.

The LC circuit acts as a filter if its impedance is much greater than the sheath's.

$$Z_{ck} \gg Z_{sh} \tag{3.10}$$

In other words, denoting the RF frequency as f, the filter is effective if Eq. (3.11) is valid.

$$f = \frac{1}{2\pi\sqrt{L_{ck}C_{ck}}} \tag{3.11}$$

The sheath actually oscillates at several harmonics; the main contribution is due to the first harmonic, so the filter can be refined inserting in series a second filter that also cuts the second harmonic at $f_2 = 2f$.

The optimal filter in this case would be a series of four filters like the one shown in Figure (3.9) centered at the frequencies of: 1.8MHz, 2.2MHz, 3.6MHz, 4.4MHz.

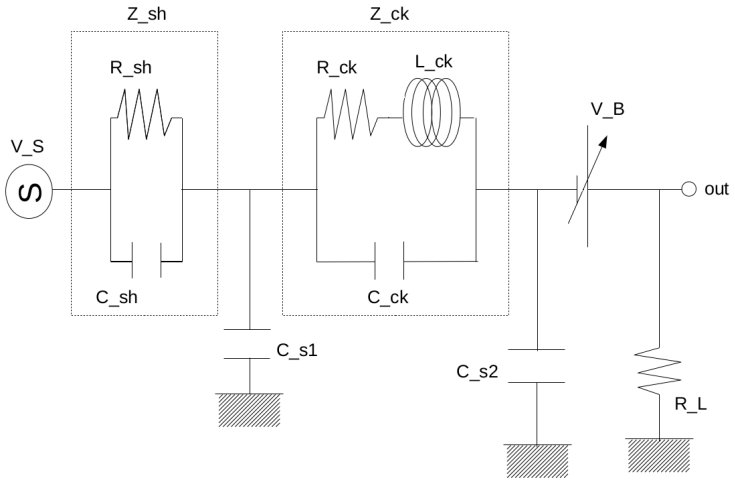

Figure 3.9: Probe Circuit with LC compensation filter

The sheath resistance depends on the plasma resistivity ρ_{el}, calculated in the case of a weakly ionised plasma with the formula provided in (16).

$$\rho_{el} = \frac{n_n \sigma_{coll}\sqrt{m_e k_B T_e}}{e^2 n_e} \tag{3.12}$$

where σ_{coll} is the collision cross section of electrons on neutrals.

$$R_{sh} = \rho\frac{10\lambda_D}{\pi a^2} \tag{3.13}$$

In the case of a planar probe, the sheath capacitance can be calculated considering the sheath as a plane capacitor with plate area πa^2 and plate distance $10\lambda_D$.

$$C_{sh} = \frac{\epsilon_0 \pi a^2}{10\lambda_D} \tag{3.14}$$

The equivalent impedance of the sheath at the frequency f is Z_{sh}.

$$Z_{sh} = \frac{1}{\frac{1}{Z_C} + \frac{1}{Z_R}} \tag{3.15}$$

where $Z_C = \frac{1}{2\pi f C_{sh}}$ and $Z_R = R_{sh}$.

The values obtained for low and high pressure regimes are shown in Table (3.1).

	pressure [Pa]	R_{sh} [mΩ]	C_{sh} [pF]	Z_{sh} [mΩ]
low pressure regime	0.1	0.3	0.5	0.3
high pressure regime	10	0.2	3.7	0.2

Table 3.1: Sheath circuit parameters

The filter circuit equivalent impedance Z_{ck} is shown in Eq.(3.16).

$$Z_{ck} = \frac{1}{2\pi f C_{ck} + \frac{1}{2\pi f L_{ck}}} \tag{3.16}$$

The values of L_{ck} and C_{ck} will be chosen to satisfy both the requirements of Eq. (3.10) and (3.11).

3.3 Effects due to other charged species

The I-V probe characteristic can be modified by the presence of spurious charged species collected together with electrons and positive hydrogen ions.

3.3.1 Negative hydrogen ions

Negative hydrogen ions H^- effect will be most evident for measurements performed near the PG, where the major H^- production takes place. When the probe is biased at positive potentials, negative ions are collected together with the electrons. The H^- produced in the scource is at the temperature of the neutral and positive ion gas, $400K < T_0 < 600K$, so the electron transition and saturation branches the I-V curve will be a superimposition of two characteristics at different temperatures, as shown in Figure (3.10): the ideal electron characteristic at a higher temperature $T_e \sim 1eV$ and the negative ion characteristic at a lower temperature T_0. The shape of the curve may be distorted and a second knee arises in the transition region, which corresponds to negative ion saturation. The electron saturation current measured by the probe may be lower than the real value by a factor which increases with the H^- density. The negative hydrogen extracted current density has a nominal value of $j_{H^-} = 300A/m^2$. I estimated the corresponding maximum negative ion saturation current I_{H^-} collected by a planar probe of diameter a located in the extraction region and found that it is of order of the ion saturation current.

$$I_{H^-} = \frac{1}{4}\pi a^2 j_{H^-} \sim 20\ mA \tag{3.17}$$

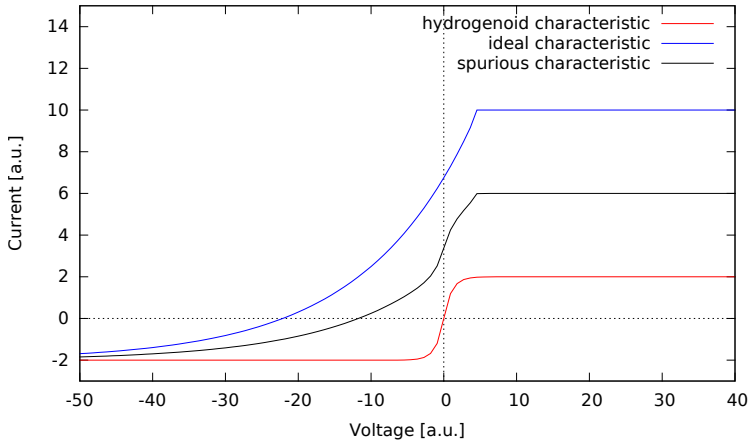

Figure 3.10: Planar probe I-V characteristic if cold H^- ions are present

Figure (3.10) shows the effect of negative hydrogen on the characteristic (black line): the ideal characteristic is distorted is shown together with the expected characteristic if the plasma were only formed of positive and negative hydrogen ions. The electron saturation current has been rescaled by a factor 1/10 to be visible. the spurious characteristic shows two different temperatures in the transition region.

3.3.2 Caesium

At present, negative hydrogen is formed in the NIO1 source by volume processes, but a caesium vapour injector is about to be installed at the rear of the plasma grid to enhance the H^- production.

Caesium deposition on the probe surface may alter its functioning and even induce short circuits between the electrode and the holder. Care must be taken in designing the electrode, in particular, the insulator between the electrode and the holder must be carved with labyrinths as will be discussed in detail Section (4.2.4).

3.3.3 Secondary electrons

When the probe is biased at high negative potentials, the ions may acquire enough kinetic energy that they extract secondary electrons when they hit the electrode surface. From data available in (17) for molybdenum, which is a typical material used for electrodes, this effect is found to be worth considering at potentials more negative than -100V. The secondary electron emission current has the appearance of additional ion saturation current. This gives rise to a greater slope below the knee and would normally be interpreted as a lower electron temperature than is actually present. To limit this effect, the probe voltage should not be swept at voltages below 100V.

Chapter 4

Design of the probe system

In the previous chapters I discussed the plasma parameters expected in the NIO1 source, their orders of magnitude and spatial gradients and determined that a suitable probe dimension that guarantees locality, planar-sheath theory applicability and good extracted signal is a=5mm. A suitable array spacing is d=15mm. I later analysed the importance of several effects on the I-V characteristic. I found that the magnetic field effect is not negligible on the electron saturation branch for both lines of sight and proposed geometric solutions to minimise the effect on the characteristic. I discussed the effect of RF electric fields on the probe characteristic and proposed methods to reduce the fluctuations and re-obtain a DC characteristic. I finally discussed the effect of collected impurities on the I-V characteristic.

In this chapter, I will present the two projects designed for the axial scan of the source and the parallel scan at the PG rear.

In the previous study of the plasma I determined constraints on the probe geometry, but the actual project must also take account of the material response to plasma, high temperature and vacuum environment, of the geometrical constraints imposed by NIO1 setup and provide solutions for the probe operation, namely the linear translation of the device and its sampling mode.

4.1 Materials

The choice of materials is limited by the environment in which the probe is to be inserted.

- **Vacuuum effect:** Since the device will be operated in high vacuum, all materials must have negligible outgassing rates. Outgassing rate is a coefficient representing in-vacuum impurity immission by a material per unit time per unit of exposed surface.
- **Temperature effect:** The materials to be employed must be able to resist temperatures of up to $250°C$.
- **Plasma effect:** The vapourisation of surfaces exposed to plasma is increased by the sputtering phenomenon. Sputtering can either be due to plasma particles (here, hydrogen) impinging on the surface and eroding material from it, or it can be self-sputtering of surface particles previously eroded from the surface. Materials should therefore have low sputtering yield.
- **Mechanical stress:** Furthermore, mechanical constraints imposed by the setup need to be considered, like for example the reduced aperture of the flange and the relative length of the holder with respect to its section, and choose materials with appropriate robustness.

An accurate study of the properties of probe materials has been carried out by (18). Using the data presented in (18), I determined the choice of materials for the probes to be used in NIO1.

4.2 Axial probe design

4.2.1 General features

The axial probe will be used to dynamically scan plasma parameters parallel to the z-axis of the chamber, from the source rear (z=-0.25 m) to the plasma grid (z=0). In this regard, it would be more useful to have an array of moving probes, rather than a single probe, so as to be able to simultaneously measure parameters at different positions.

4.2.2 Magnetic field

In Section (3.1.3) I analysed the effect of the magnetic field direction on the probe characteristic and found that for $z > -0.20m$ the field varies in intensity but the dominant component is along the x-axis. For this reason, it is best to place the probe with the surface orthogonal to the x-axis, to minimise the field effect. The $-0.25m < z < -0.20m$ interval corresponds to the source rear, where the confining magnets are placed; the magnetic field direction and intensity in this region is variable. Nevertheless, measuring here is not the main purpose of the diagnostics, the most interesting region is in fact beyond the coil, when the plasma enters the expansion region where the H^- production takes place.

4.2.3 Holder design

The probe access at the rear of the source is a CF16 type flange with an internal diameter of 12mm.

A first solution involved an insulating holder in boron nitride (BN). This was found to be unfeasible due to mechanical constraints: BN cannot be soldered nor threaded to insert blocking screws, but different parts can be fastened via dovetail joints. The reduced dimensions of the accesses would have forced to design the projecting tenon no more than 1 - 1.5 mm wide for a holder dimension of about 10mm, insufficient to resist mechanical stress. The final solution features a thin steel tube-shaped holder that acts as a coat for the other components. The holder has external and internal diameters of D=11mm e d=9mm, leaving an interspace of 0.5mm between holder and flange.

Figure 4.1: Exploded view of the holder: axial probe

Both the flange and the holder are made of steel, hence friction might become extremely high in vacuum because no impurity layer interposes to prevent the surfaces from binding. However, the level of vacuum in the chamber is not high enough for this to occur. At the minimum pressure of 0.1Pa, the gas density is $n_n \sim 10^{19} m^{-3}$; taking the cube root of the density we obtain a rough estimate of the number of particles per unit length: $\sqrt[3]{n_n} \sim 10^3 mm^{-1}$, which is high enough for the interspace to effectively act as a cushion.

Another issue concerning the holder is its possible thermal volume expansion. Between the chamber (holder) and the outside (flange) there can be a temperature gradient of $\Delta T \approx 200°C$; considering the volume expansion of a tube-shaped holder (radii r=4.5mm, R=5.5mm, thickness b=1mm) with a linear thermal expansion coefficient $\alpha_{lin} = 1.07 \cdot 10^{-5} K^{-1}$ (19), we obtain: $\Delta b = b \cdot \alpha_{lin} \cdot \Delta T \approx 2 \cdot 10^{-3} mm$ in the radial direction and $\Delta R = R \cdot \alpha_{lin} \cdot \Delta T \approx 11 \cdot 10^{-3} mm$ raising from the circumference expansion; the sum of the two variations is still not enough to overgrow the flange radius.

4.2.4 Electrode design

The electrode will be built in TZM, a molybdenum-based refractory alloy able to withstand current collection in a plasma. Another possibility was to design steel electrodes, but given the limited diameter of the access flange, the electrode would have been too thin to resist long-life operation in the plasma at the maximum absorbed power, but this solution could work for low absorbed power operation.

A section of the electrode with relevant dimensions is shown in Figure (4.2).

- **blue:** electrode
- **light grey:** holder
- **yellow:** insulators
- **dark grey:** nut
- **black:** conducting disc

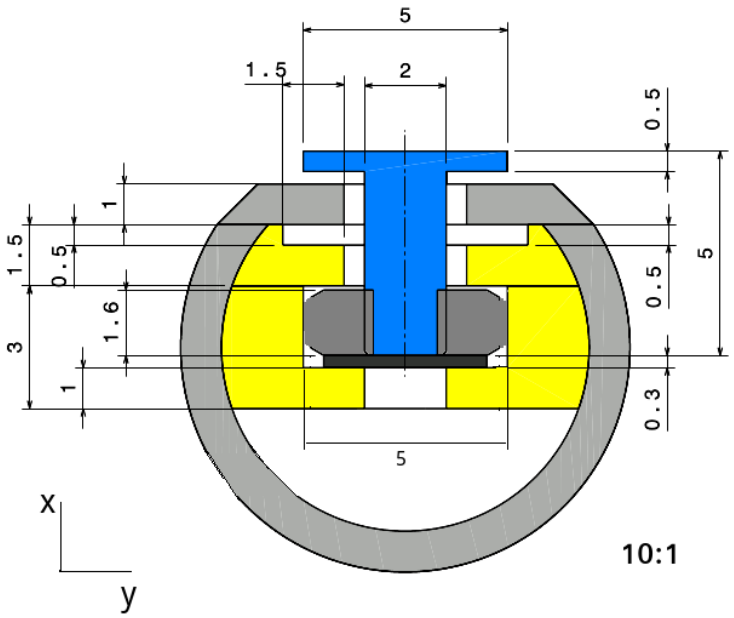

Figure 4.2: Axial electrode section with dimensions in mm units

Current collection
The electrode is a TZM screw with a disc-shaped top as active surface for the current collection. The diameter of the disc was chosen considering the axial limit on measurement averaging discussed in Section (2.4). An electrode diameter of 5 mm is suitable for the purpose: the density relative error ϵ_n in the axial direction is below 20%, whereas the temperature profile is affected by a relative error below 8%.

The difficulty in using TZM consists in the fact that it cannot be directly soldered to metal cables, so other methods have to be developed to ensure the electric contact. The electric contact is mantained screwing the electrode in a steel nut which sits on a 0.3mm-thick conducting disc. Once tightened, the screw rests on the disc to whose lower surface the cables can be direcly soldered. I chose to adopt the screw-nut solution because of geometry constraints, in fact a first design featured a hollow TZM electrode containing a spring pressed to the conducting disc, simular to the system designed in (14); this solution however was found to be unfeasible since the spring would have had to be only

1mm in diameter and the insulating discs would have been too thin and challenging for fabrication.

Since the holder is made of a conducting material, the gap between the electrode and the holder must be as small as possible. This is because the breakdown potential as given by Paschen's formula depends on the pressure-gap product. As we see from Figure (4.3), for a pressure of 1Pa and a gap of 0.5mm, we obtain $(pd) = 3.5 \cdot 10^{-}4cm \cdot Torr$, which corresponds to a very high breakdown potential, $V_{break} > 1kV$. The gap must also be small to prevent the source plasma from diffusing towards the insulators.

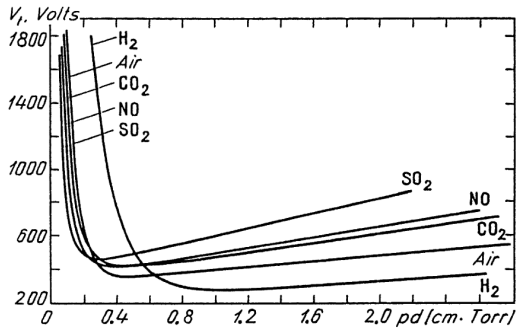

Figure 4.3: Paschen curve, from (20)

Insulation
The nut and disc are enclosed between two insulating structures in Macor®. As shown in Figure (4.4), the lower structure is carved to house the disc and nut: the housing shape is a rounded rectangle which blocks the nut from turning; in the absence of this precaution, it would be impossible to tighten the screw.

The upper structure is carved with labyrinths whose function is to hinder spurious metal deposition. The carving does not need to be elaborate; it is sufficient to create a "blind bend" which sputtered particles cannot directly reach. The presence of the labyrinths is essential especially because the H^- production in NIO1 will be driven by caesium: without them, caesium might deposit on the surface and produce a short-circuit.

4.2.5 Probe setup

The probe setup is shown in Figure (4.5): in the longitudinal direction the upper part of the cylinder holder surface (orthogonal to the x-axis) is flat and features an array of four holes with a 15mm spacing between the centres. The array spacing is chosen taking into account the considerations of Section (2.4): the insulatig structures containing the nuts and discs will be assembled separately and then inserted into the cylinder. The TZM electrodes will be screwed through the cylinder holes as a final step of the probe assembling. The cylinder-insulator structure will be fixed by a screw. The lower part of the cylinder is hollow and acts as a passage for the four probe cables.

4.2.6 Wiring

All cables employed are suitable for in-vacuum operation with temperatures up to 260°C. Given the presence of the RF source, all wiring must also be insulated. The cables chosen are Caburn's Kapton® KAP4 coaxial cables, with a jacket diameter of 1.47mm. The stray capacitance of KAP4 is $C_s = 300\ pF/m$.

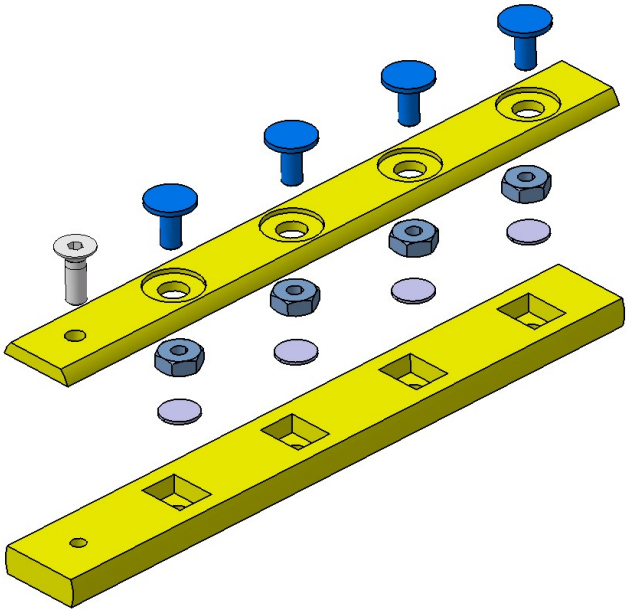

Figure 4.4: Exploded view of the insulator: axial probe

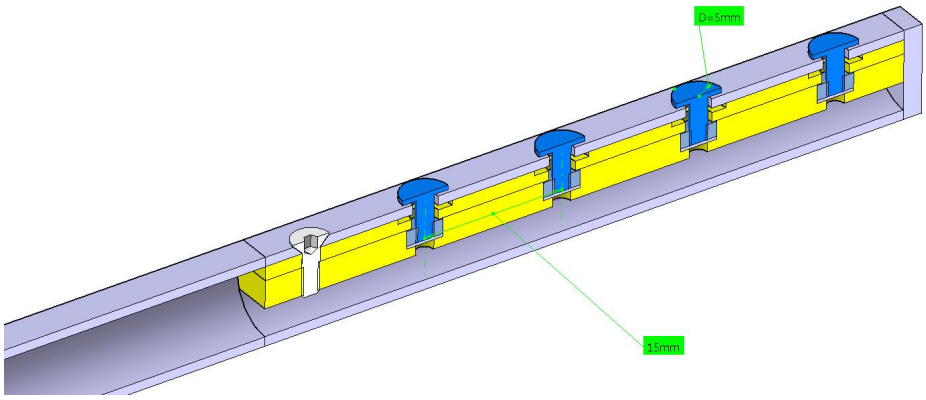

Figure 4.5: Axial probe setup section

4.2.7 RF compensation circuit

As discussed in Section (3.2.1), the probe needs a compensating circuit to eliminate RF fluctuations. The values of L_{ck} and C_{ck} must satisfy Eq.(3.11) but at the same time the dimensions of the capacitor and the inductance must be small enough to fit in the holder. The filter should in fact be placed as near as possible to the electrode to minimise stray capacitance introduced by the wiring. For a RF frequency of f=2MHz, suitable values for the capacitance and the inductance lie on the graph shown in Figure (4.6).

Capacitors and inductances with suitable values and dimensions are commercially available.

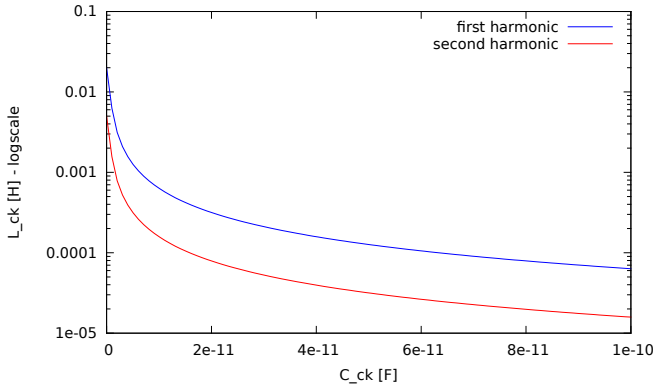

Figure 4.6: Filtering condition

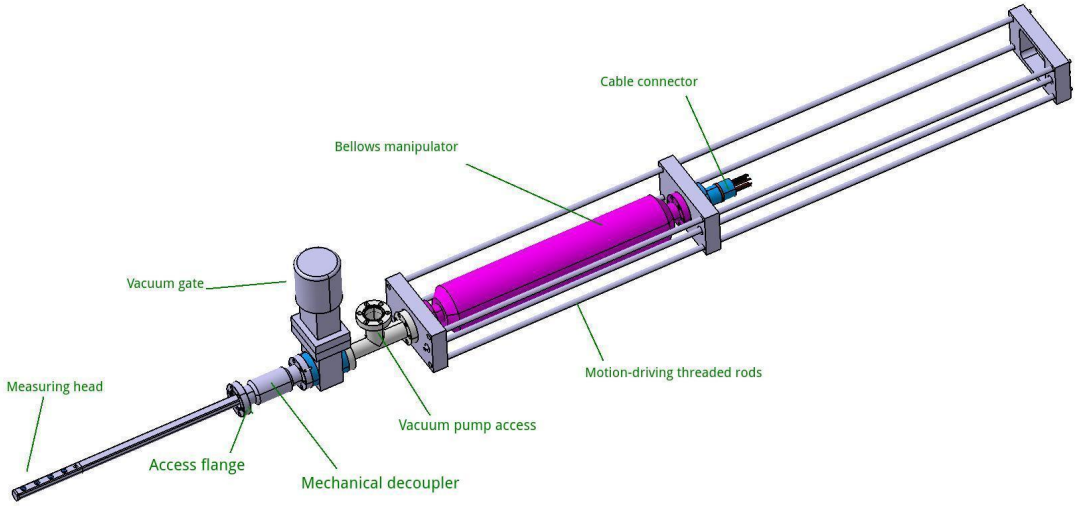

Figure 4.7: Manipulator setup: axial probe

4.2.8 Manipulator

The probe must be able to scan the whole length of the chamber, from the rear of the source (z=-0.25 mm), to the plasma grid (z=0). Even if the NIO1 source plasma environment is not as harsh as that of fusion plasma, where the electron temperature can be of order 1keV, it is not advisable to keep the probe inside the source for a long time: this in order to preserve the probe, but also to protect the plasma from eccessive impurity inlet by probe erosion. For the source operation, I designed a system which uses a bellows manipulator to drive the probe into the chamber and out until it is completely extracted.

The manipulator setup is shown in Figure (4.7).

- **Mechanical decoupler:** it consists of a short bellows tube (70mm); without it, vibrations might extend into the chamber and cause serious damage to the apparatus.
- **Vacuum gate:** the measuring head will be withdrawn until the gate, so as to be allowed to remove the probe for mantainance without interfering with the HV regime of the chamber.
- **Vacuum pump:** it controls the pressure inside the bellows system.

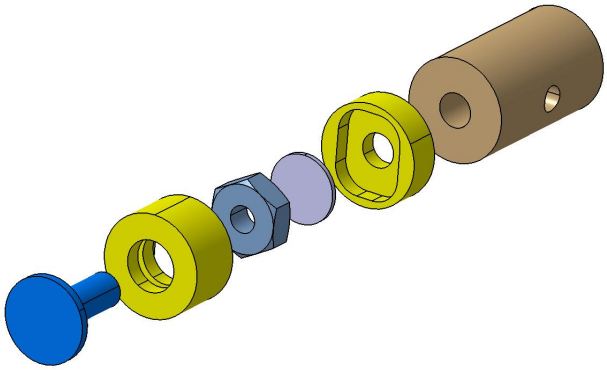

Figure 4.8: Exploded view of the insulator: PG probe

- **Bellows manipulator (500mm + 180mm):** It is a compressible tube made with a series of "concertina" metal badges which can be pressed up to a minimum length, typically 30-40% of the effective stroke. During operation, the pressure in the bellows is the same as that in the chamber. The manipulator stroke has been designed to be 500mm, which is sufficient for a complete scan and extraction of the probe.
- **Motion-driving threaded rods:** they drive the bellows expansion or contraction and also prevent it from collapsing under the pressure difference with the atmosphere.
- **Cable connector:** it is the outlet at which the signal is picked up to be analysed.

4.3 Plasma Grid probe design

4.3.1 General features

The PG probe will be inserted parallel to the plasma grid at a distance of 20mm and scan along the radius of the chamber. Its design is simpler than that of the axial probe, in the sense that it does not require the array structure and the length to scan is only 0.08m, but is complicated by the fact that the diameter of the available access is only 8mm.

4.3.2 Magnetic field

The magnetic field along the probe line of sight varies considerably in magnitude but its direction lies on the xy-plane, being the z-component of the field almost zero (see Fig.(3.1.a)). Unfortunately, because of the smaller flange size, there is no other solution than designing the probe with the surface orthogonal to the radial direction. The cross-section of the magnetic field on the probe suface will vary along the radius, but the magnetic field profile is actually known from simulation so the effect is always quantifiable.

4.3.3 Electrode design

The electrode design is analogous as in the case of the axial probe. The electrode is a 5mm-diameter TZM screw and the electric contact is ensured by the nut-disc structure. The structure of the two Macor® cylinders enclosing the nut-disc, as displayed in Figure (4.8), is slightly different to increase its resistance to mechanical stress.

The electrode section is shown in Figure (4.9).

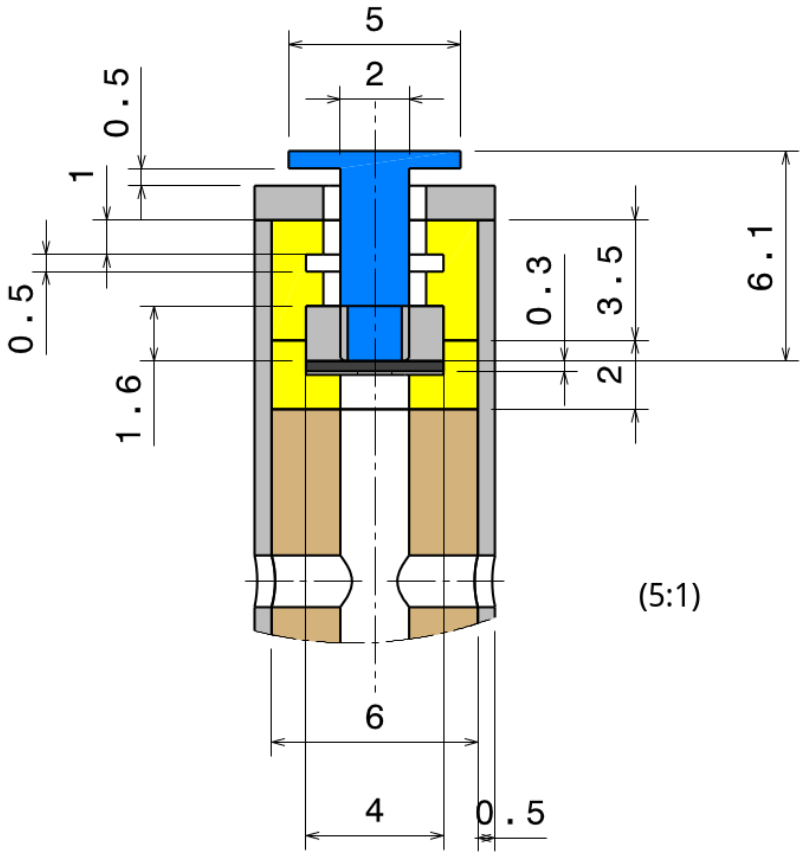

Figure 4.9: PG electrode section with dimensions in mm units

4.3.4 Probe setup, manipulator and circuit

The insulator-contact structure is to be assembled separately and later inserted in the cylinder shaped holder. At the bottom of the cylinder a soldered perforated disc blocks the insulators; in the other direction the structure is blocked by a thick brass perforated cylinder 1mm long. The holder and the brass cylinder are blocked via two screws. The blocking cylinder should not be made of steel because of the friction effect discussed before in (4.2.3).

The same strategy developed for the axial probe is still valid for the PG probe, except for the fact that the total stroke of the manipulator only needs to be 150mm.

The complete setup of the probes together with a section of NIO1 is shown in Figures (4.12),(4.13), (4.14).

4.4 Data sampling methods

The I-V probe characteristic will be constructed sweeping the probe bias voltage V_B with a triangular-shaped wave. A reasonably low frequency to obtain DC plasma parameteres is 20kSample/s. In this way the curve can be fitted via minimum-squares methods to calculate plasma parameters. Such a low frequency does not allow to follow the 2MHz RF fluctuations, nor to study wave propagation in the plasma; besides, this is not the main aim of the diagnostics, which is in fact to study plasma uniformity, electron density and temperature in the source and in particular in the PG region.

The probe should not be swept at voltages below -100V to avoid secondary electron

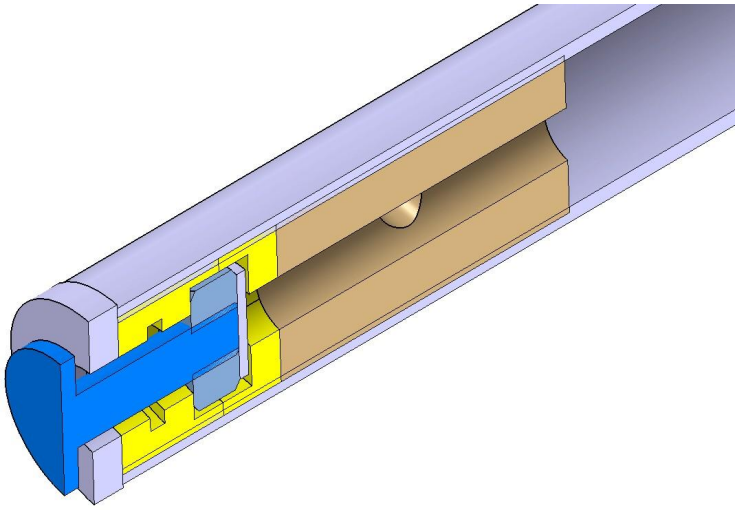

Figure 4.10: Section of the probe setup: PG probe

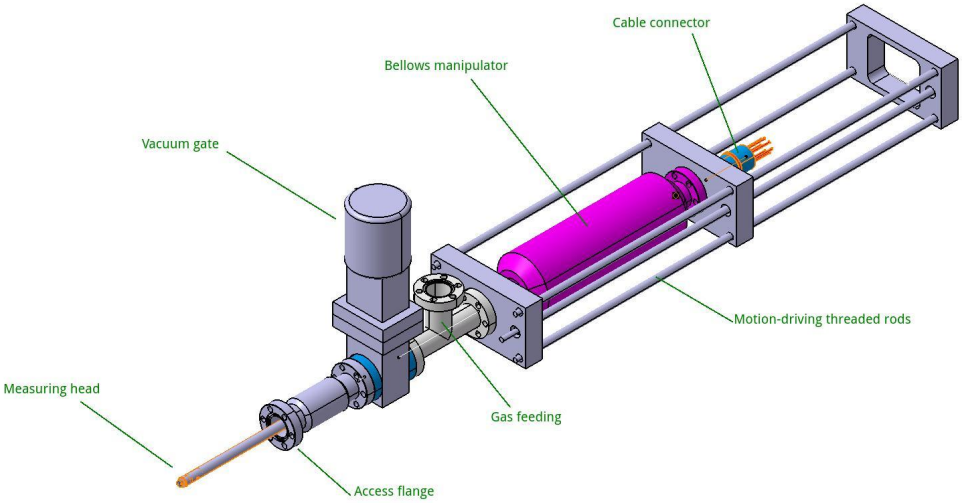

Figure 4.11: Manipulator setup: PG probe

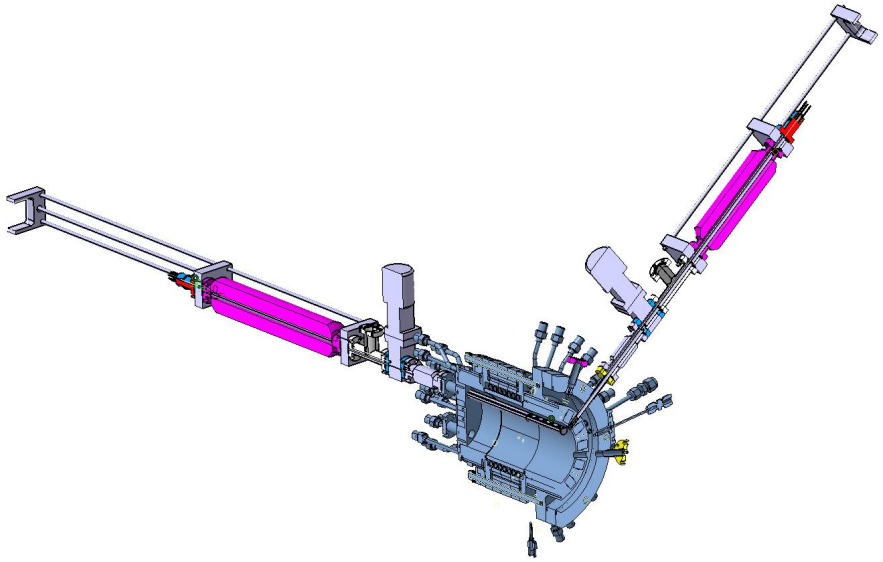

Figure 4.12: Complete probe setup: overview

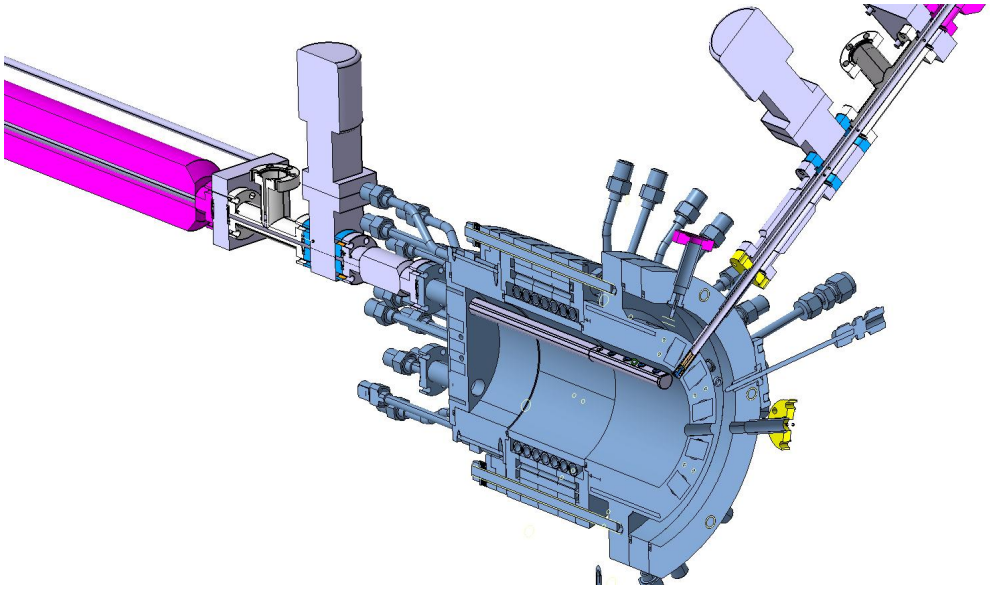

Figure 4.13: Complete probe setup: chamber scan

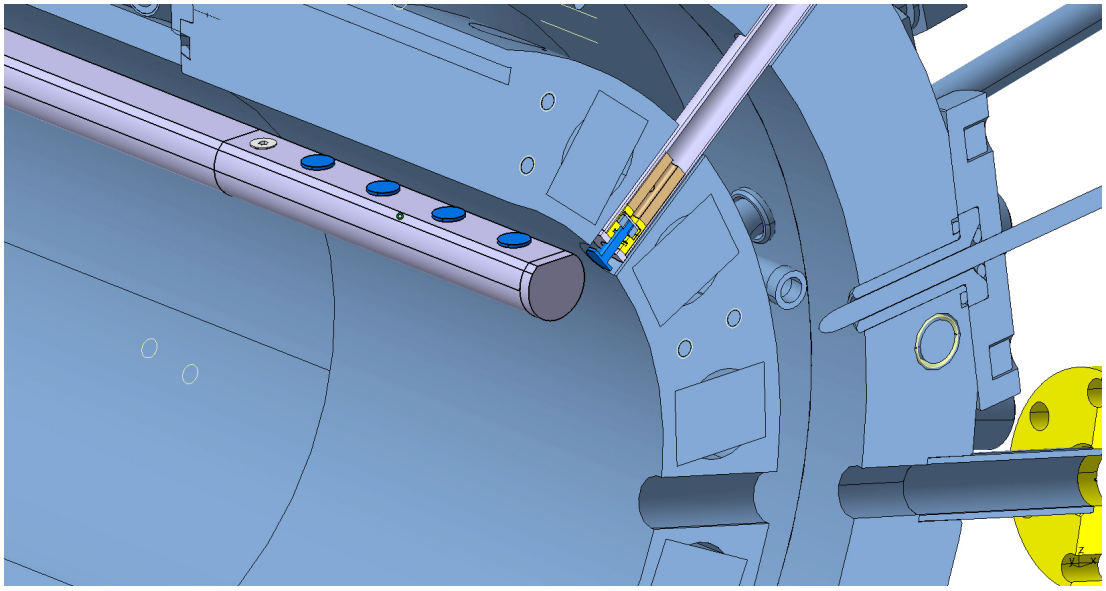

Figure 4.14: Complete probe setup: particular of the measuring heads

emission, nor at very high voltages; the electron saturation branch is in fact the most affected by fluctuations and distortion phenomena.

Chapter 5

Conclusions

The NIO1 radiofrequency negative ion source is a facility built at Consorzio RFX, Padova, with the aim of understanding the optimal configuration for negative ion sources to be used on the ITER fusion experiment. A thorough diagnostics of the plasma parameters in the source is essential. In particular, a system of electrostatic probes was designed in this work.

The requirements imposed by the nature of the NIO1 source plasma have been studied in order to determine the optimal probe design for both the axial probe and the PG probe. After analysing the electron density and temperature profiles for different operation regimes, it was found that the optimal probe dimension is 5mm; this analysis also enabled us to define the array spacing for the axial probe to be 15mm.

After studying the magnetic field effect, a solution was proposed to minimise it for the axial probe, designing it to be oriented with its surface orthogonal to the x-axis of the chamber. Owing to constraints imposed by the setup, the PG probe has to be oriented with its surface orthogonal to the line of sight for the probe.

An anti-resonant LC filter circuit was designed to minimise 2MHz RF fluctuation due to inductive coupling in the source.

The appropriate materials for the probe were defined: the holder will be made of steel, the electrode will be built in TZM, a molybdenum alloy, and the insulators will be made of Macor®.

The electrodes and measuring heads were designed considering also geometrical constraints of the apparatus.

Finally, the system of electrostatic probes was successfully designed including an axial probe, a probe parallel to the PG and their relative manipulation mechanisms and operation methods.

Bibliography

[1] M. Kikuchi, K. Lackner, and M. Tran, *Fusion Physics*. IAEA: International Atomic Energy Agency, 2012.

[2] ITER, "www.iter.org/."

[3] I. Brown, *The physics and technology of ion sources*. Wiley-VCH, 2 ed., 2004.

[4] M. Cavenago, T. Kulevoy, S. Petrenko, G. Serianni, V. Antoni, M. Bigi, F. Fellin, M. Recchia, and P. Veltri, "Development of a versatile multiaperture negative ion source," *Review of Scientific Instruments*, vol. 83, no. 2, 2012.

[5] R. Hippler, S. Pfau, M. Schmidt, and K. H. Schoenbach, *Low Temperature Plasma Physics*. WILEY-VCH, 2001.

[6] M. Cazzador, M. Cavenago, G. Serianni, and P. .Veltri, "Semi-analytical modeling of the nio1 source," *presented at 4th International Symposium on Negative Ions in Muenchen*, October 2014. accepted for publication in AIP Conference Proceedings.

[7] M. Cazzador, "Analytical and numerical models and first operations on the negative ion source nio1," Master's thesis, University of Padua, Dept. of Physics and Astronomy, 2014.

[8] B. Zaniol *et al.*, "Nio1 diagnostics," *presented 4th International Symposium on negative Ions in Muenchen*, October 2014. accepted for publication in AIP Conference Proceedings.

[9] H. Tawara *et al.*, "Cross section and related data for electron collisions with hydrogen molecules and molecular ions," *J.Phys.Chem.Ref.Data*, vol. 19, no. 3, p. 620, 1990.

[10] T. Tabata and T. Shirai, "Analitic cross sections for collisions of hydrogen and hydrogen molecules," *Atomic Data and Nuclear Data Tables*, vol. 76, pp. 12–25, 2000.

[11] M. Liebermann and A. Lichtengerg, *Principles of plasma discharge and material processing*. Wiley - Interscience, 2 ed., 2005.

[12] A. Boschi and F. Magistrelli, "Effect of a rf signal on the characteristic of a langmuir probe," *Il Nuovo Cimento*, vol. 29, no. 2, 1963.

[13] M. Brombin, M. Spolaore, G. Serianni, *et al.*, "Electrostatic sensors for spider experiment: Design, manufacture of prototypes, and first tests," *Review of Scientific Instruments*, vol. 85, no. 02A715, 2014.

[14] M. Spolaore, G. Serianni, A. Leorato, and F. D. Agostini, "Design of a system of electrostatic probes for the rf negative ion source of the spider experiment," *J. Phys. D: Applied Physics*, vol. 43, no. 124018, 2010.

[15] I. Sudit and F. Chen, "Rf compensated probes for high-density discharges," *Plasma Sources Sci. Technol.*, vol. 3, 1994.

[16] F. Chen, *Introduction to plasma physics and controlled fusion.* Plenum Press, 2 ed., 1974.

[17] E. W. Thomas, *Data compendium for plasma surface interaction*, ch. Secondary electron emission, p. 102. special edition, Journal of Plasma Physics and Thermonuclear Fusion, 1984.

[18] A. Leorato, "Progetto di un sistema diagnostico basato su sonde di langmuir per sorgenti di ioni negativi impiegate in iniettori di fasci di neutri," Master's thesis, University of Padua, Dept. of Electrical Engineering, 2008.

[19] M. Okaji, N. Yamada, and H. Moriyama, "Ultra-precise thermal expansion measurements of ceramic and steel gauge blocks with an interferometric dilatometer," *Metrologia*, vol. 37, no. 2, p. 170, 2000.

[20] Y. P. Raizer, *Gas discharge physics.* Springer-Verlag, 1991.